

# **UNIVERSITY OF SOUTHAMPTON**

**Faculty of Engineering, Science and Mathematics**

**School of Electronics and Computer Science**

**Design, manufacturing and testing of a vibration powered  
piezoelectric generator**

**By**

**MARIOS STAMOS (ms8v07)**

**Completed at 18<sup>th</sup> September 2008**

**A dissertation submitted in partial fulfilment of the degree of**

**MSc. Microelectronics and Systems Design**

**By examination and dissertation**

**Supervisor: Dr Steve Beeby**

**Examiner: Dr Paul H Chappell**

## Abstract

*As modern industries continue to develop, a constantly increasing need arises for continuous monitoring of potentially hazardous working environments via the use of embedded wireless sensor networks or any other type of monitoring equipment. The immediate problem created from such complex networks is the provision of a constant supply of power. A solution to this problem is the introduction of energy harvesting generators. This document consists of the design, manufacturing and testing processes of a series of thick film piezoelectric generators. The generators were designed for future placement on helicopter blades and were developed to satisfy the energy generation requirement of the European Union TRIADE project. ANSYS Finite Element Analysis was applied to produce candidate architectures which led to the creation of a series of cantilever beam devices. Actual manufacturing was done by using thick film (screen printing) process. As part of the thick film process, a novel tungsten ink was formulated and deposited to act as the inertial mass of the device. The tested generators provided with a useful power output of  $9.3\mu\text{W}$  under  $0.1\text{m/s}^2$  of acceleration.*

## Acknowledgements

I would like to thank Dr. Steve Beeby, my supervisor, for his support and friendship towards the completion of this MSc. Thesis.

Special thanks to Dr. Russel Torah for offering me his assistance, experience and valuable time in critical stages of this project.

## Table of Contents

Abstract .....	2
Acknowledgements .....	2
I. Chapter 1: Introduction .....	5
I.I Introduction.....	5
I.II Thesis structure .....	5
II. Chapter 2: Energy harvesting and thick-film principles .....	6
II.I Energy harvesting .....	6
II.II Vibration powered generators .....	6
II.III Piezoelectric generator constants .....	7
II.IV TRIADE Project.....	8
II.V Thick-film printing (screen printing).....	9
III. Chapter 3 : Design phase .....	10
III.I ANSYS modelling.....	10
III.I.I Resonant frequency aim.....	10
III.I.II ANSYS devices.....	11
III.I.III ANSYS electro coupled analysis .....	14
III.I.IV Alternative device architectures .....	15
III.II L-edit substrate and screen designs .....	16
III.II.I Stainless steel substrate etching masks .....	16
III.II.II Thick film process screens .....	18
III.III Inventor substrate holder and device clamp designs.....	19
III.III.I Substrate holder .....	19
III.III.II Device clamps .....	20
IV. Chapter 4 : Screen printing phase .....	22
IV.I Screen printing ink preparation.....	22
IV.II Mass ink.....	22
IV.III Screen printer preparation .....	23
IV.IV Dielectric layer (ESL4924) .....	24
IV.V Bottom Electrode layer (ESL8836).....	25
IV.VI PZT layer (PZT-5H) .....	26
IV.VII Top electrode layer (ESL1901-S).....	27
IV.VIII Mass layer (custom made polymer tungsten ink).....	27
V. Chapter 5: Testing .....	29
V.I Polarisation.....	29
V.II Vibration generator testing .....	29

VI.	Chapter 6: Cost and time analysis .....	33
VI.I	Cost analysis .....	33
VI.II	Time analysis .....	33
VII.	Chapter 7: Conclusion and suggestions for further work.....	35
VII.I	Suggestions for further work.....	35
VII.II	Conclusion .....	35
VIII.	Appendices .....	36
IX.	References .....	58

# **I. Chapter 1: Introduction**

## **I.I Introduction**

The EU TRIADE project consists of a research attempt, funded by the European Union, to create an autonomous sensing device with power generation, storing and data transmission capabilities for continuous health monitoring of helicopter vehicles. The existence of this project led to the initiative of experimenting with the power generation requirements of the TRIADE project in an attempt to create a piezoelectric generator device capable of providing enough power to allow operation of any given sensor.

As part of the development of the piezoelectric generator the author was required to investigate on design modelling and Finite Element Analysis by using appropriate simulation tools provided by the University of Southampton. Specific limitations such as the maximum deflection and maximum device size were also provided to the author in order to allow for better device design. A series of different architectures was investigated which led to the design of two different device substrates which were brought forward for manufacturing.

For creation of all piezoelectric devices, the thick film process (screen printing) method was selected as part of investigating a low cost fabrication process. During device manufacturing, a novel polymer tungsten ink was formulated and used to create a mass volume on the devices. For deposition of all remaining materials, individual thick film screens were also designed.

Finally, all devices were placed on a vibration generator and connected with load resistance in order monitor the power output. For mounting the devices on the vibration generator, custom made clamps were designed for every different chip design.

## **I.II Thesis structure**

Chapter two of this thesis is concentrated on design and simulation. The first section of chapter two is mainly investigation with ANSYS which is presented in consequent steps that the designer has made that led to the finalization of the piezoelectric generator's architecture. The design work described in this section was made by collaboration with Miss Charlene Nicoleau. The second section is devoted on the L-edit designs of the substrate etch masks and all thick-film screens which were used during manufacturing of the devices. The final section of this chapter is a description of the custom made test clamps which were used during testing of the devices and the substrate holder design used at the manufacturing phase.

All practical work towards manufacturing of piezoelectric devices is described in chapter three. Different formulations of tungsten inks were tested by deposition on alumina substrates and firing at suitable temperatures. Density measurements were performed on ideal structures to determine the most suitable material for final device deposition. Furthermore all problems involved in manufacturing are described in this chapter together with the actions performed by the author to overcome these issues.

Chapter four is a description of the testing processes involved for measuring the performance of the devices. Such processes involved polling of the devices, mounting on the vibration generator and all different tests performed on the experimental devices. All acquired results are presented in the same chapter together with Appendix J. Testing of the devices was performed by collaboration with Miss Charlene Nicoleau.

Finally chapters five and six conclude the achievements of the author by presenting evidence of time and resource management through a project cost and time analysis. Suggestions for future work are also provided together with reflections on methods to improve the performance and quality of devices for aiding future academic research.

## II. Chapter 2: Energy harvesting and thick-film principles

### II.I Energy harvesting

Recent years have demonstrated an increase of embedded wireless sensors comprising vast and complicated continuous monitoring networks. As health and safety regulations are constantly being reviewed and updated, industries across the country are forced to enhance their safety procedures by continuously monitoring the operation of possible harmful environments. Applications such as the interior of nuclear reactors, high temperature environments or even the stress development on fast moving vehicles are making use of monitoring networks [1].

This extensive use of sensing nodes has led to the creation of the problem of powering up every individual node. Despite the fact that advances in Integrated Circuit manufacturing have produced sensor designs which are able to operate on extremely economical profiles of well below 1 mW[2], frequent battery replacement would still be required at a rate of one battery per 8000 hours of operation for an electronic device consuming 100 $\mu$ W [3]. Considering the prohibited cost of wired power and continuous battery replacement, an alternative solution exists in the form of energy harvesting.

Energy harvesting makes use of ambient sources of energy, existing in the surrounding environment such as vibrations, acoustic noise or temperature variations, in order to produce electric power. An advantage of energy harvesting over traditional power mechanisms is that ambient energy can be potentially constant in the surrounding environment thus providing power to any attached sensor. Alternatively, an energy harvesting device can be connected with a storing charge capacitor structure thus providing a continuous recharge to a battery. Furthermore, due to the fact that there are no replaceable components, energy harvesting devices consist of the most financially attractive solution over the long run with minimum impact to the environment.

### II.II Vibration powered generators

As per described in section II.I, numerous energy harvesting devices are utilizing different ambient energy sources in order to produce a level of output power. This thesis will only focus on the analysis and presentation of vibration powered generators. Mechanical vibrations can be harvested via the use of miniaturized generators based on electromagnetic [4-7], electrostatic [8-10] and piezoelectric [11-15] conversion.

The overall structure of an energy conversion generator is based on the operation of a first order resonant generator model (figure 1). A seismic mass  $m$  is used to model the combined effect of the actual mass of the system together with any effective mass added by reactive load circuits. The spring stiffness  $k$ , represents the actual physical spring of the system with any effective spring added by the electrical load. In order to initiate movement, an excitation  $y(t)$  is applied to the generator which results in differential movement between the mass and the housing  $z(t)$ . The energy in the system is removed by both unwanted sources of loss (such as gas damping), and taken away as useful electrical power. The different types of damping are represented by a viscous damping coefficient  $C_T$  [16].

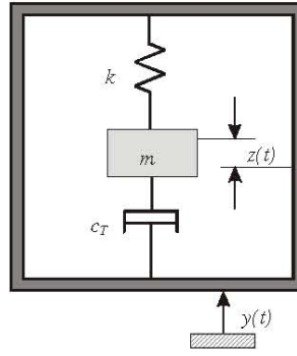


Figure 1 Inertial generator linear model [16]

Furthermore for an oscillating beam, the maximum generated power can be predicted by using

$$P_d = \frac{ma^2}{4\omega_n\zeta_T}$$

Where  $P_d$ ,  $m$ ,  $a$ ,  $\omega_n$  and  $\zeta_T$  are total damped power (W), mass (kg), acceleration ( $\text{ms}^{-2}$ ), resonant frequency (rads) and total damping respectively. In order to maximize the mechanical power the inertial mass and it's amplitude of vibration should be maximized [17].

### II.III Piezoelectric generator constants

Despite the fact that each individual energy conversion method has its advantages and disadvantages, a direct comparison of the energy density of each type clearly reveals that piezoelectric generators are capable of producing the highest power output [18].

Type	Energy density ( $\text{mJ cm}^{-3}$ )	Equation	Assumptions
Piezoelectric	35.4	$(1/2)\sigma_y^2 k^2 / 2c$	PZT 5 H
Electromagnetic	24.8	$(1/2)B^2 / \mu_0$	0.25 T
Electrostatic	4	$(1/2)\epsilon_0 E^2$	$2 \times 10^7 \text{ V m}^{-1}$

Table 1 Summary of maximum energy densities of three kinds of transducers [18]

Where  $\sigma_y$  is the yield stress,  $k$  is the coupling coefficient,  $c$  is the elastic constant,  $B$  is the magnetic field,  $\mu_0$  is the permeability of free space,  $\epsilon_0$  is the permittivity of free space, and  $E$  is the electric field.

Piezoelectric generators are utilising active materials which when subjected to mechanical strain they tend to become electrically polarized where the degree of polarization is proportional to the applied strain. Additionally, active piezoelectric materials tend to deform when exposed to an electric field. Some examples of piezoelectric materials are single crystals (e.g. quartz), piezoceramic (e.g. lead zirconate titanate or PZT), thin film (e.g. sputtered zinc oxide), screen printable thick-films based upon piezoceramic powders and polymeric materials such as polyvinylidenefluoride (PVDF).

A series of constants in conjunction with the axes notation can determine the level of piezoelectric activity of a material.

The piezoelectric strain constant,  $d$ , is defined as:

$$d = \frac{\text{strain developed } m}{\text{applied field } V}, \quad (1)$$

$$d = \frac{\text{short circuit charge density } C}{\text{applied stress } N} \quad (2)$$

Depending on the axis of the compressive strain; generators that rely on a strain perpendicular to the electrodes, are exploiting the  $d_{33}$  coefficient whilst others, which apply a transverse strain parallel to the electrodes are exploiting the  $d_{31}$  coefficient.

An equally important constant is the electro-mechanical coupling coefficient,  $k$ . This constant describes the efficiency with which the energy is converted by the material between electrical and mechanical forms in a given direction. The electro-mechanical coupling coefficient is defined as:

$$k_{ij}^2 = \frac{W_i^e}{W_j^m} \quad (3)$$

Where  $W_i^e$  is the electrical energy stored in the  $i$  axis and  $W_j^m$  is the mechanical input energy in the  $j$  axis.

Furthermore,  $\eta$  is the efficiency of energy conversion for a piezoelectric element clamped to a substrate and cyclically compressed at its resonant frequency. It is defined as:

$$\eta = \frac{\frac{k^2}{2(1-k^2)}}{\frac{1}{Q} + \frac{k^2}{2(1-k^2)}} \quad (4)$$

Where  $Q$  is the quality factor of the generator. It is obvious from equation four that the efficiency can be improved by increasing  $k$  and  $Q$  [19].

## II.IV TRIADE Project

As per described in section II.I, energy harvesting devices can be implemented in extreme working environments in order to supply power to sensor devices. The project described in the main body of this document was an experimental approach to partially satisfy the power generation requirements of the ongoing EU TRIADE project. The main target of the project is to identify and realise an integrated device which should be capable of power generation, power conservation, intelligence-data processing /storage and energy management for performing Structural Health Monitoring in aeronautical applications [20]. In addition to the substantial cost savings occurring from reducing the continuous inspections of the integrity and health of vehicle parts, Structural Health Monitoring is effectively increasing the safety of the personnel since a mechanical or otherwise failure can be immediately identified and treated accordingly.

The current concept for realising the TRIADE project is the fabrication of the smart tag. This device will include a battery, an antenna, an RF inductive coupling link, a memory, an energy harvesting part, a power management circuit and a microprocessor. The dimensions of the smart tag should not exceed the size of a credit card (8.5cmX5.4cm). All individual building blocks will use state of the art technology to ensure maximum performance and low power requirements. The device target cost should not exceed 100€ [20].

In order to ensure the minimum fabrication cost of the energy harvesting block, the screen printing process was selected for manufacturing a vibration based piezoelectric generator. The target dimensions of the generator were identified ideally as half the size of a credit card (4.25cmx5.4cm), to allow for incorporation of the remaining elements after being embedded on the smart tag.



## II.V Thick-film printing (screen printing)

Thick-film technology (screen printing) has originally been created for producing hybrid circuits which consisted of monolithic silicon chips, thin films, discrete components and thick films [21]. Thick film technology is based on the deposition of different materials which originally have the viscosity of a paste. These formulations are created according to application need and consist of a mixture of different reagents. The different materials are deposited in layers on top of a substrate which is required to be aligned with the layer's screen.

The process can be separated in four different phases:

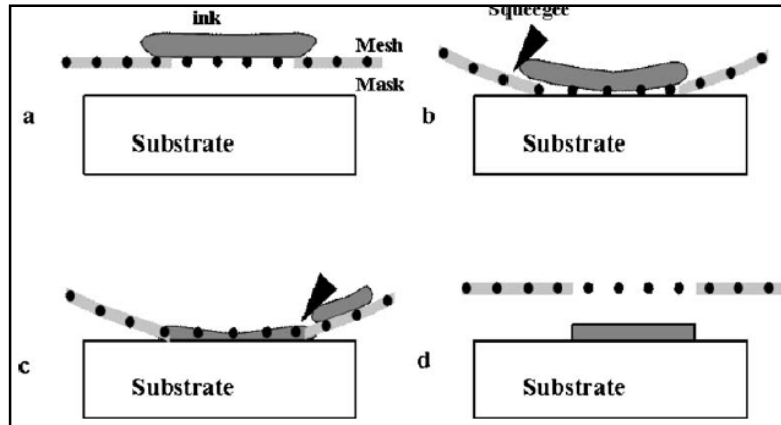


Figure 2 Process steps for screen-printing [22]

Step a) of the screen printing process, involves spreading the formulated paste across the screen via the use of a flood blade. In step b) a polyurethane squeegee forces the screen down on to the substrate as it begins the print stroke. The squeegee is then drawn across the screen thus forcing the paste through the etched sections of the screen and removing the excess paste. Finally the pressure is removed and the screen returns to its original position [22].

It is important to consider that the printing pressure, the gap between the screen and the substrate and the viscosity of the paste are responsible for controlling the thickness of the printed layer. For subsequent printed layers the gap size is required to be increased to ensure that the screen can return to its original position without smearing the print [22].

Minimum feature size and geometry available are the limitations of the conventional screen-printing. For every different material deposited as part of this project, a separate pattern was created which was then transferred to a  $\mu$ -screen. A  $\mu$ -screen consists of a very fine custom etched mesh mounted on a conventional screen frame [23]. Information about the different material patterns as well as the screen specifications are provided at section III.II.II.

### III. Chapter 3 : Design phase

#### III.I ANSYS modelling

Due to the already proven piezoelectric efficiency, the devices were decided to be based on an already existing structure design where PZT active material is deposited on a stainless steel substrate, separated via a dielectric layer. Top and bottom electrodes are placed parallel to the PZT layer. All the fore mentioned layers are deposited on both sides of the substrate with screen printing. Further information on the experimental results of figure 3 test device, are provided in [24].

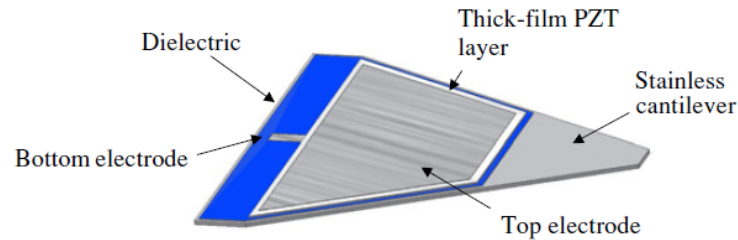


Figure 3 Tapered thick-film PZT generator (not to scale) [19]

Initially, investigation was focused on the creation of a simple orthogonal cantilever device. Such an approach would allow for an easier learning curve of Finite Element Analysis with the use of ANSYS. ANSYS is capable of designing complete 3D models by element type materials with different mechanical, thermal and electrical properties. Furthermore upon completion of the design, ANSYS can perform F.E.A in order to evaluate stress development and produced electric potentials [25].

##### III.I.I Resonant frequency aim

In order to produce a successful architecture, experimental results were provided from a test flight with a helicopter vehicle.

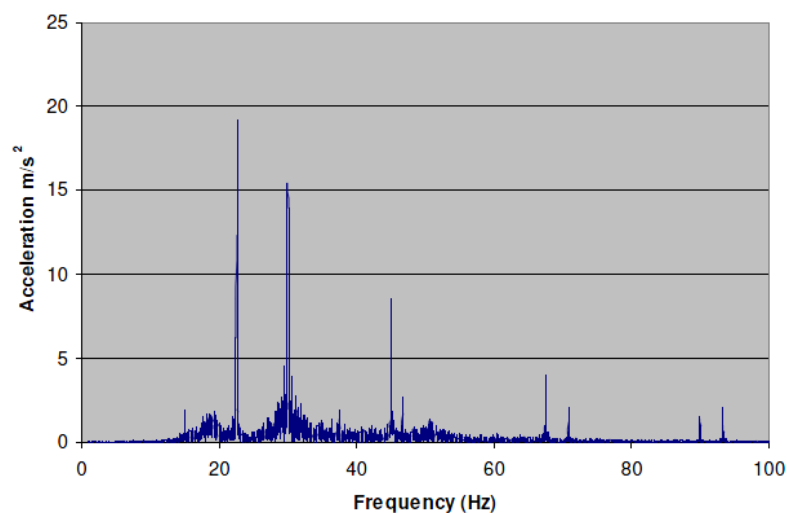


Figure 4 Vibration frequency spectra on a helicopter vertical stabilizer (Diagram provided by the flight test department, PZL Swidnik S.A., Poland)

From figure 4, it is possible to observe that high acceleration peaks exist at 23Hz, 30Hz, 45Hz, 67Hz and 93Hz. Although it would be possible to design individual devices, each one addressing to a different level of acceleration, it was decided that a more sensible approach was to design three devices targeting key frequencies throughout the frequency spectra. Although the highest peak occurs at 23Hz, due to the acceleration value and narrowness of the frequency spectra, construction of a device targeting this

frequency would be difficult to create. An engineering decision was made to use as resonant frequency targets, 30Hz, 45Hz and 93Hz.

A resonant frequency analysis was performed based on the simple beam cantilever model in order to calculate reference beam dimensions which could be compared with the generated dimensions from the ANSYS models, by using the formula

$$f_n = \frac{(k_n l)^2}{2\pi l^2} \left( \frac{\int_h E(z - z_0)^2 dz}{\sum_{i=1}^N (h_i \rho_i)} \right)^{\frac{1}{2}}$$

Where  $k$  = modal parameter,  $l$  = length of cantilever,  $h$  = thickness of layer,  $\rho$  = density of material and  $E$  = young's modulus. For further information the reader is forwarded in Appendix A.

### III.I.II ANSYS devices

In order to be able to validate the designed architectures, the designer decided to create each individual device in a 3D representation by using firstly the Element type Solid 45. According to ANSYS user manual: "SOLID45 is used for the 3-D modelling of solid structures. The element is defined by eight nodes having three degrees of freedom at each node: translations in the nodal  $x$ ,  $y$ , and  $z$  directions. The element has plasticity, creep, swelling, stress stiffening, large deflection, and large strain capabilities." Such an element would therefore allow for a modal analysis in order to get the resonant frequency of operation of the device.

For an individual device, each layer was required to be created as a separate volume which comprised of lines specified via coordinate key points in the  $x$ ,  $y$  and  $z$  direction. Although this process was rather tedious and repeatable, it allowed for full control over the produced model and numbering of every created volume. Due to the nature of ANSYS, this process was more beneficial in terms of getting familiar with how ANSYS operates with the active model.

For every different material used, a set of mechanical properties was required as an ANSYS input in order to perform the F.E.A. (table 2). In figure 5 it is possible to observe the cross-sectional layer of the simple cantilever design consisting of all required layers.

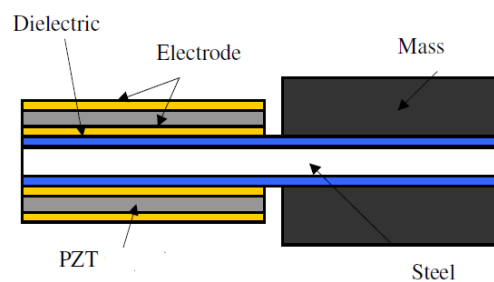


Figure 5 Device printed cross section [26]

Material	Young's modulus(Pa)	Poisson's Ratio	Density(kg/m <sup>3</sup> )	Source References
Stainless steel Substrate 430s17	$2 \times 10^{11}$	0.26	7750	[27]
Glass Dielectric Pyrex 7740	$0.64 \times 10^{11}$	0.2	2230	[28]
Gold electrode	$0.8 \times 10^{11}$	0.42	19280	[29]

Tungsten mass	$3.4 \times 10^{11}$	0.24	15000	[29]
Piezoelectric Active layer PZT-5A	$1.15 \times 10^9$	0.3	7750	[30][31]

Table 2 ANSYS mechanical properties input

Each volume was bind to the corresponding material thus assigning the relevant mechanical properties to the structure.

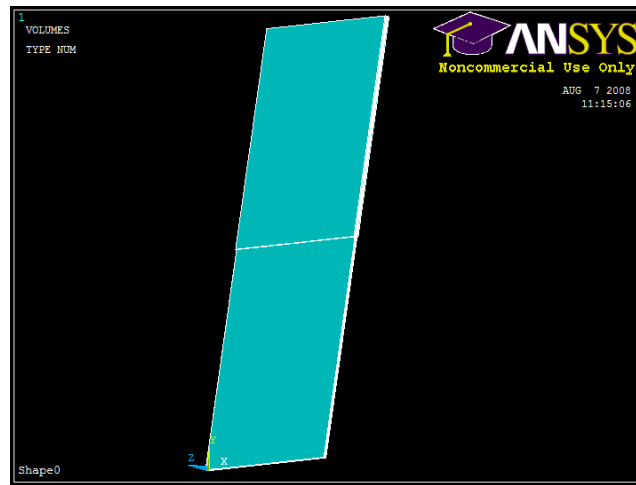


Figure 6 Simple cantilever structure

Figure 6 consists of an example simple cantilever structure. For simplification reasons the mass volume was decided to be adjacent to the PZT volume. Such a decision would not have a major impact on the overall frequency of operation and was necessary due to ANSYS errors during volume designing.

In order to be able to perform Finite Element Analysis, all volumes were required to be meshed by elements. ANSYS provides a smart size meshing tool which is able to perform unmapped meshing to the structure. This method is based on calculating the smallest possible element that can be placed in the structure and meshing the entire structure with this element. The size of the element depends on the size and dimensions of the structure and the level of smart size refinement selected by the user [32]. Figure 7 consists of the meshed structure by using the smart tool and selecting smart size 10. However this meshing method had as a result the production of numerous elements which made any F.E.A. impossible to compute due to the lack of memory resources.

An alternative solution was the performance of mapped meshing. Mapped meshing required the division of each specified volume line by the number of required elements. Although this process was more time consuming it led to a satisfactory meshed structure which was able to produce a legitimate resonant frequency value (figure 9).

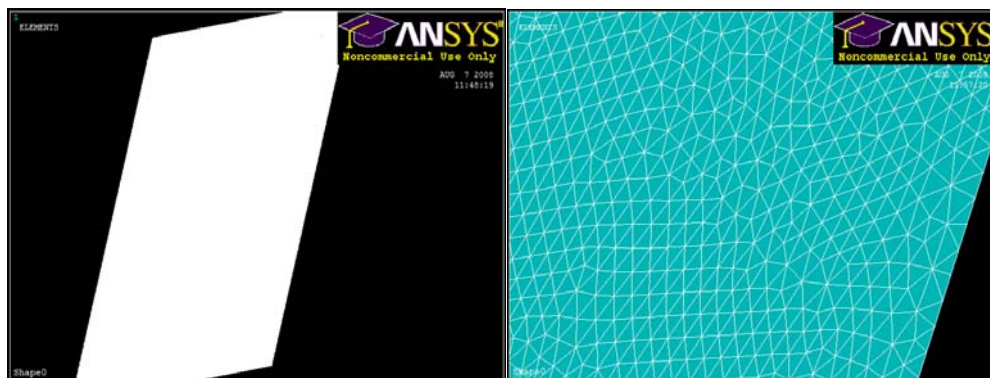


Figure 7 Smart size meshed simple cantilever structure

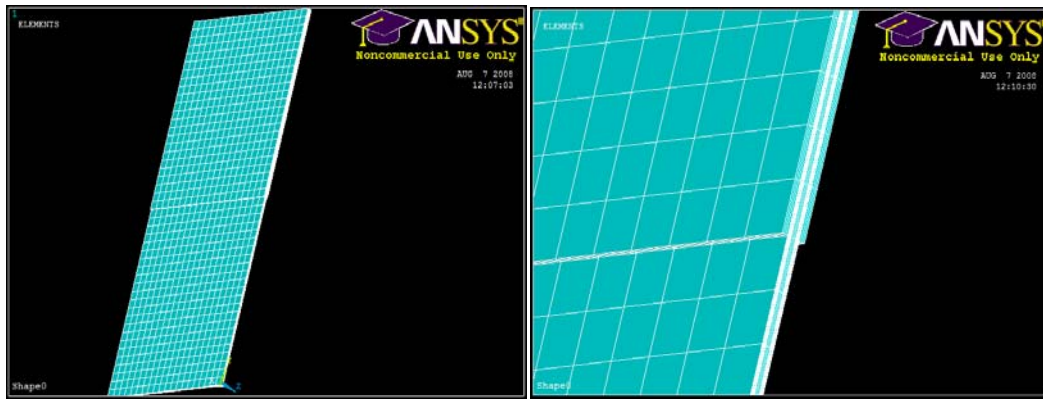


Figure 8 Map meshed simple cantilever structure

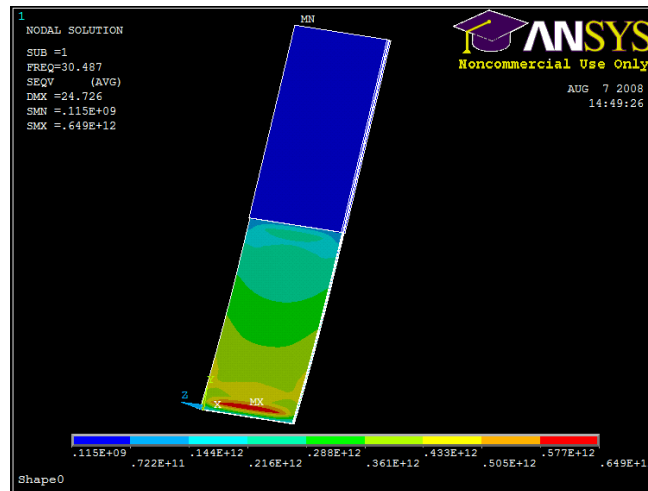


Figure 9 Modal analysis on a simple cantilever beam

Several modal analyses with the same structure and different levels of meshing produced different resonant frequency results. Therefore an alternative method of designing the structure was applied by using element type SHELL 99. According to ANSYS user manual SHELL 99 may be used for layered applications of a structural shell model. SHELL 99 allows up to 250 layers and has six degrees of freedom at each node. The structure designed by using SHELL 99 can be thought as a 2D representation of a 3D object where the specified area has the mechanical properties of all different material layers. Such an approach not only provided another validation source but it required fewer areas to be created, thus making meshing and computation time much less compared to SOLID 45 structures.

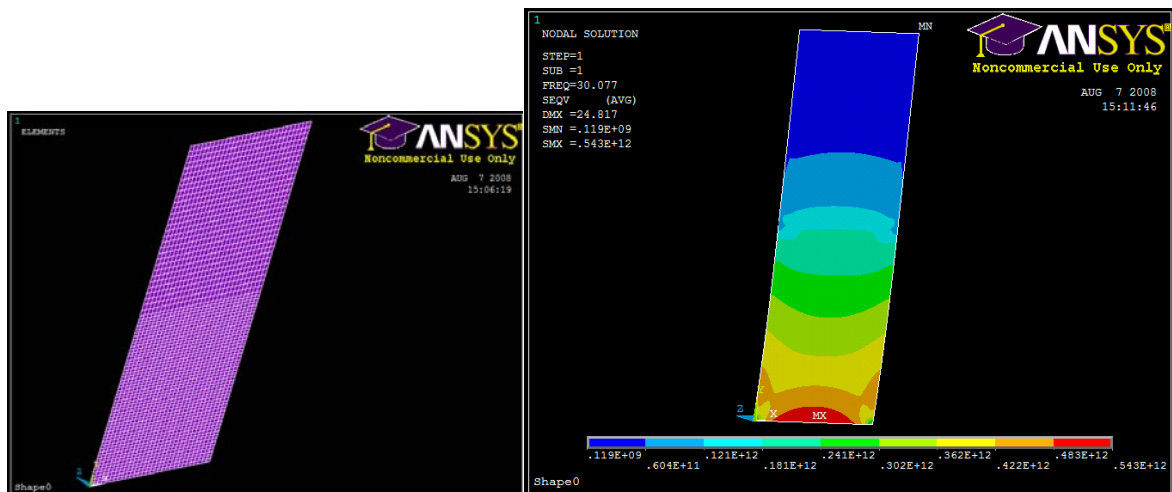


Figure 10 SHELL99 meshing and modal analysis of a simple cantilever structure

Detailed experimental simulations are analysed in Appendices B and C. Example ANSYS code written models are included in Appendix CD.

### III.I.III ANSYS electro coupled analysis

In order to perform an electro coupled analysis, piezoelectric properties were required to be entered for the PZT material. According to [31], for PZT-5A.

PZT constants	Value
Relative permittivity (k) in X at constant strain	916
Relative permittivity (k) in Y at constant strain	830
Relative permittivity (k) in Z at constant strain	916
Piezoelectric stress coefficient $e_{33}$ ( $\text{m}^2/\text{C}$ )	15.8
Piezoelectric stress coefficient $e_{31}$ ( $\text{m}^2/\text{C}$ )	-5.4
Elastic stiffness coefficient $c_{33}$ ( $10^{10}\text{N}/\text{m}^2$ )	11.1
Elastic stiffness coefficient $c_{33}$ ( $10^{10}\text{N}/\text{m}^2$ )	12.1

Table 3 PZT-5A piezoelectric properties

The corresponding ANSYS PZT volumes were bind with the new piezoelectric properties. Furthermore, the top electrodes were coupled with the voltage property so that any generated voltage could be measured, while the rest of the structure was grounded. Finally acceleration values were taken from figure 4 for the corresponding frequencies and programmed in ANSYS.

Frequency (Hz)	Acceleration ( $\text{m}/\text{s}^2$ )
30	15.44
45	8.611
93	2.01

Table 4 Corresponding acceleration at 30, 45,93Hz

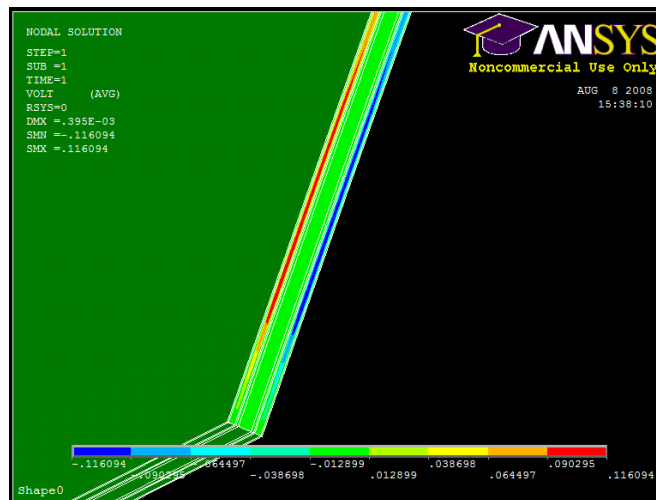


Figure 11 Example generated voltage for the 30Hz cantilever beam design

Further simulations and rectifications in beam structure are presented in Appendix D. The generated voltage for the final beams is presented in table 5.

Device Characteristics	Shell 99 model frequency (Hz)	Solid 45 model frequency (Hz)
100 $\mu\text{m}$ sub+2diel 20 $\mu\text{m}$ +4elec 10 $\mu\text{m}$ +2PZT 50 $\mu\text{m}$ +2mass 200 $\mu\text{m}$ , W=2cm, Lm=2.5/5*L		
A:L=4.68cm	29.90	30.30
B:L=3.84cm	44.90	45.50
C:L=2.68cm	92.70	94.10

DEVICE A: 30Hz (acceleration at 15.44 m/s <sup>2</sup> )	Value
DMX (max deflection in m)	3.86x10 <sup>-4</sup>
SMN (minimum generated voltage in V)	-1.322x10 <sup>-1</sup>
SMX (maximum generated voltage in V)	1.322x10 <sup>-1</sup>

DEVICE B: 45Hz (acceleration at 8.611 m/s <sup>2</sup> )	Value
DMX	9.65x10 <sup>-5</sup>
SMN	-4.699x10 <sup>-2</sup>
SMX	4.699x10 <sup>-2</sup>

DEVICE C: 93Hz (acceleration at 2.01 m/s <sup>2</sup> )	Value
DMX	5.24x10 <sup>-6</sup>
SMN	-4.449x10 <sup>-3</sup>
SMX	4.449x10 <sup>-3</sup>

Table 5 Displacement and generated voltage for final cantilever beam devices

Appendix E consists of a theoretical calculation of the efficiency and produced power of a PZT cantilever beam proving that the efficiency of a generator exploiting the  $d_{33}$  coefficient is higher than a generator operating based on the  $d_{31}$  coefficient.

#### III.I.IV Alternative device architectures

In addition to the simple cantilever beam, a series of alternative device architectures was considered throughout the design process.

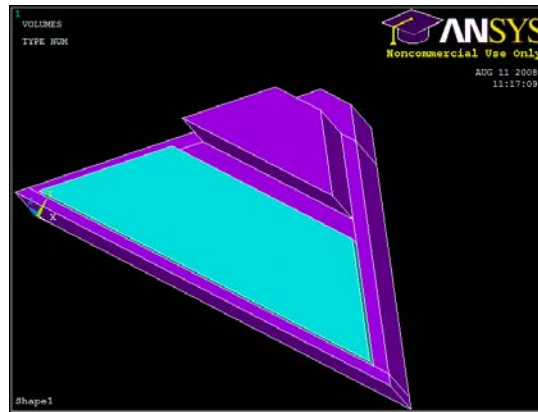


Figure 12 Trapezoid shaped device architecture

This early approach was an attempt to replicate an already existing design as presented in [19]. This design was created to take advantage of the fact that the tapered profile will have a constant strain in the piezoelectric film along its length for a given displacement. Due to the fact that the target frequency was achieved with the cantilever beam design and that multiple architectures would increase the overall cost of the project significantly, it was decided to abandon any further investigation for development of this specific architecture. However, the partial work on this particular device enhanced the designer's ANSYS design skills. Despite the fact that the triangular device architecture was dismissed, a novelty thought occurred which led to the design of a meandrical structure as depicted in figure 13.



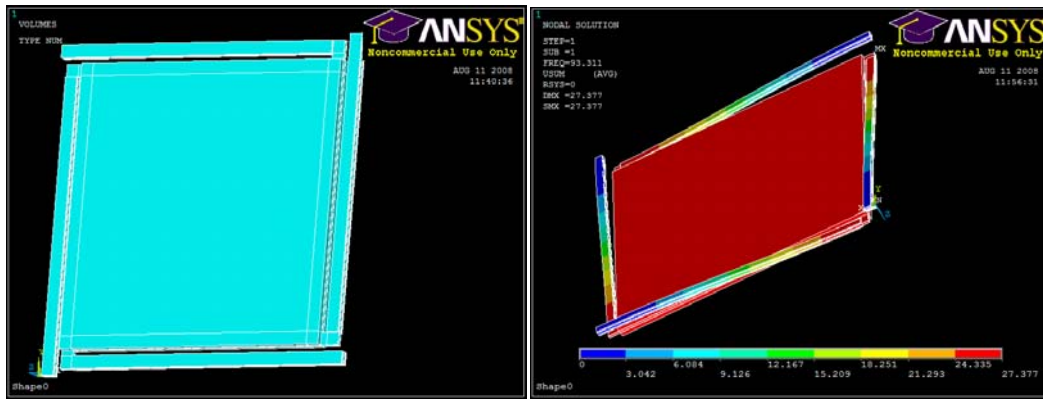


Figure 13 Meandrical architecture modal analysis

This device design consists of four cantilever beams which support a central mass. The PZT material is deposited on top and bottom of the beam area. The advantage of this design is based on the fact that the central mass allows for a higher deflection of the cantilever beams, thus potentially providing a large power output.

Device Characteristics	Shell 99 model frequency (Hz)
100 $\mu$ m sub+2diel 20 $\mu$ m +4elec 10 $\mu$ m+2PZT 50 $\mu$ m+2mass 200 $\mu$ m	
L=2cm	47.85
L=2.5cm	26.80
L=2.4cm	29.80
L=2.2cm	37.36
L=2.1cm	42.15
L=2.15cm	39.65
L=20.5cm	44.90
L=1.6cm	85.81
L=1.55cm	93.31
L=1.56cm	91.70

Table 6 Meandrical device final dimensions

## III.II L-edit substrate and screen designs

### III.II.I Stainless steel substrate etching masks

The designed cantilever beam architectures together with the meandrical structure were required to be etched on a stainless steel 430s17, 100 $\mu$ m thickness substrate. L-edit design software was proven to be more than adequate for designing the substrate mask. Considering the fact that 100mm diameter substrates were offered from A.C.E. Company, only a limited number of devices could be designed to be etched on one substrate. A decision was therefore made to include on one substrate all three single cantilever beam designs with the addition of one meandrical device. During placement of the devices, a 5mm distance rule from the substrate edge was applied. In addition 3mm circular alignment aids were placed in four key points on the substrate. Finally for every device an extra space of 4mm was added for future clamping of the device on a test mechanism and a space of 3.5mm was added for the electrode pads. For the substrate design, two masks were implemented. The second mask contained several one square millimetre tags which were drilled during the testing phase and separated each device from the substrate. The resulting substrate masks can be observed in figure 14.



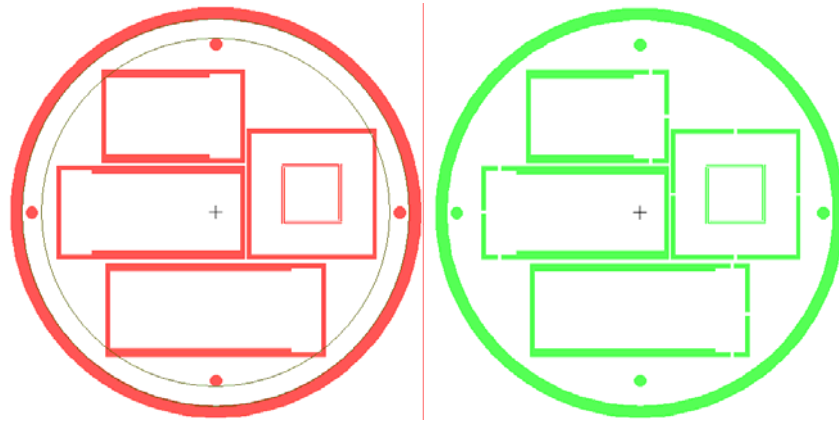


Figure 14 Individual devices, top and bottom substrate etch masks

In addition to every single device operating independently, an important experiment was considered to be the performance inspection of all cantilever beams operating into a single chip. Since every beam structure operates at a different frequency, the combination of all three structures could result to a better power output. Therefore a second set of substrate masks was created with the optimum position of all three cantilevers thus ensuring the minimum used space (figure 15).

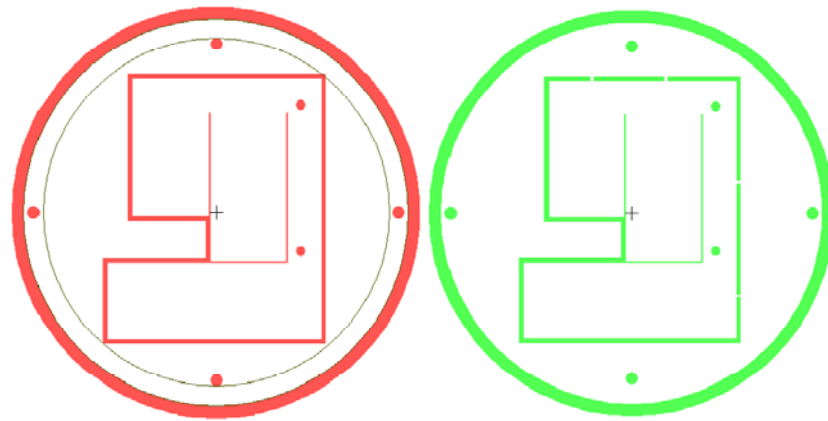


Figure 15 Three beam cantilever chip, top and bottom substrate etch masks

All L-edit designs were exported as GDSII files and with the assistance of Link CAD software, were converted to DFX files for manufacturing.

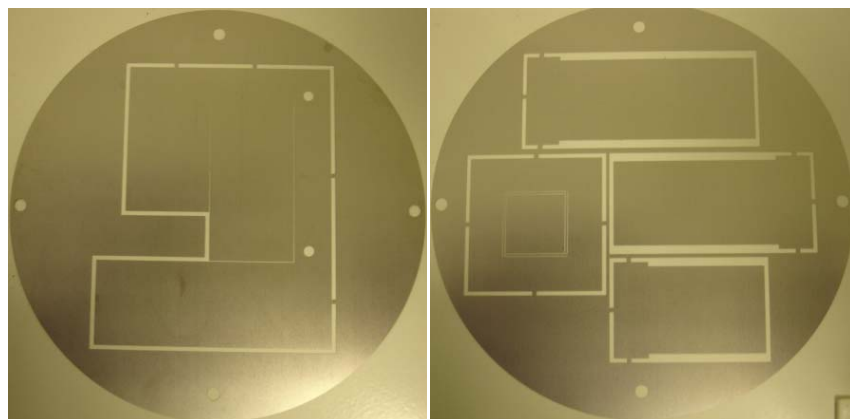


Figure 16 Etched substrates

### III.II.II Thick film process screens

Due to the fact that the substrate design was not symmetrical, a decision was made to include two different designs on each screen consisting of a normal top down and a mirror image of the design. Although this decision was the most cost-effective solution, it increased the actual printing time since constant realignment was required. In addition to four alignment aids in key positions of the screen pattern design, a minimum limit of 250 $\mu$ m reduction in size for every hierarchical layer was established in order to account for any misalignment during printing (figure 17). Due to the limitation of substrate space, this rule was omitted for the meandrinal structure.

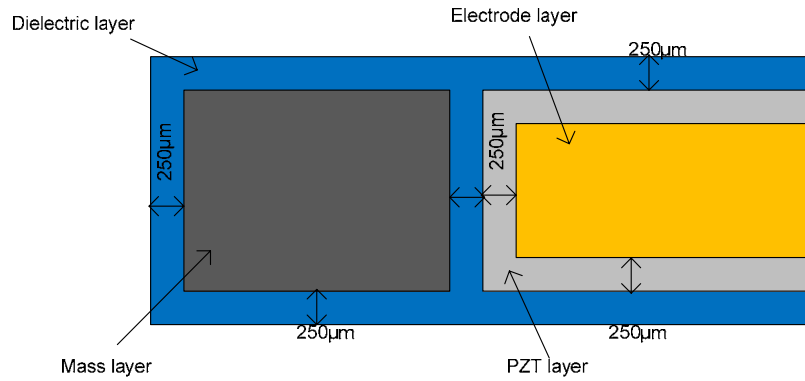


Figure 17 250 $\mu$ m design rule

For testing of the generator devices, supporting clamp structures were manufactured to hold the generators on top of a vibration generator mechanism. Therefore an effective design approach was required to isolate the bottom and top electrodes from touching the aluminium clamp. Solution to this problem was the extension of the PZT layer on top of the bottom electrode thus effectively acting as an isolation layer between the electrode and the supporting clamp.

In addition, a problem could arise when a step structure layer was being deposited. A step between two layers could have as a result the omission of certain sections of the layer due to the difference in height. Such an example is the printing of the top electrode layer. Due to the step caused by the PZT layer the top electrode could potentially not be printed (figure 18 (a)).

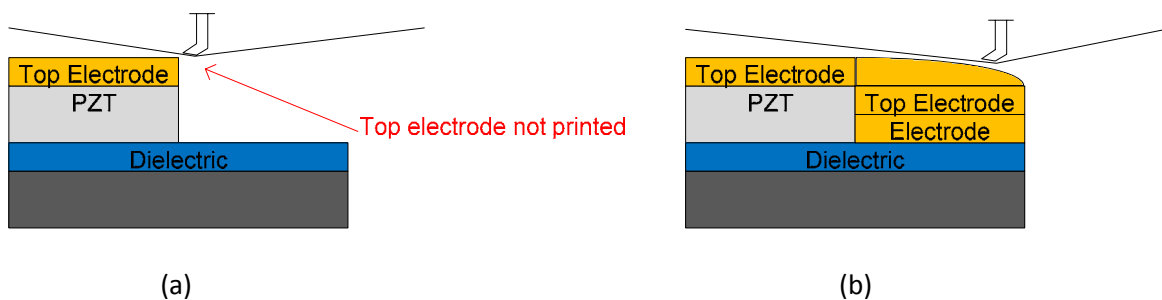


Figure 18 a) Printing problem due to step structure b) Implemented step structure solution

A solution to this problem was the design of a section of the top electrode in the bottom electrode screen. Therefore the difference in height would be significantly smaller and the top electrode would be printed without any problem (figure 18 (b)).

Overall, seven different screens were designed for each substrate. For a more detailed representation the reader is forwarded in Appendix F. Upon successful screen design, all schematics were exported as GDSII files and converted once more using Link CAD, to Gerber files for manufacturing by MCI Cambridge Ltd. All L-edit design produced files are included in Appendix CD.

In order to create the screens, a mesh size specification was required to be provided. The size depended entirely on the resolution of the finest feature on the screen. A wire cloth for screen printing guide, provided by BOPP SD Applications [33], offered a variety of different wire cloth types together with a brief tutorial to calculate the appropriate one, based on the intended application. Furthermore, the thickness of the emulsion placed on the screen was also an influence factor towards the thickness of the printed layer. Consultation of the guide and discussion with university academic staff led to the final screen specifications as presented in table 7.

Layer	Cloth type	Emulsion ( $\mu\text{m}$ )	GDSII number	G. filename
Mass	SD 140/65 per inch 120	50	7	L7
Dielectric (ESL4924)	SD 90/40 per inch 200	25	3	L3
PZT	SD 90/40 per inch 200	25	5	L5
All electrodes (ESL8836)	SD 53/24 per inch 325 (325UT)	25		
Bottom electrode	SD 53/24 per inch 325 (325UT)	25	4	L4
Top electrode	SD 53/24 per inch 325 (325UT)	25	6	L6
IDT 200 $\mu\text{m}$ electrode	SD 53/24 per inch 325 (325UT)	25	9	L9
IDT electrode	SD 53/24 per inch 325 (325UT)	25	8	L8

Table 7 Screen specifications

### III.III Inventor substrate holder and device clamp designs

#### III.III.I Substrate holder

During screen printing, each substrate was required to be aligned with the mounted screen in order to successfully deposit every material on the required location. For making this alignment process easier and more accurate the screen printer was equipped with a vacuum pump which was connected to a plastic holder. A slot provided on the plastic holder allowed for any custom made substrate holders to be mounted.

For the needs of this project, a customized substrate holder was designed via the use of Autodesk Inventor. The designed substrate holder consisted of an aluminium square surface of 6mm thickness. On the surface of the holder, a series of 1mm holes has been drilled together with the four 3mm alignment aid holes. The purpose of the alignment aid holes was to insert four rods of 3mm diameter during printing to assist the alignment of the substrate to the substrate holder. All 1mm holes were decided to be placed around the substrate chips since the suction of the pump, resulting from a hole directly under the chip device, could potentially damage a printed layer. The position of the holes was suitable for both substrates. The resulting substrate holder can be observed in figure 19.

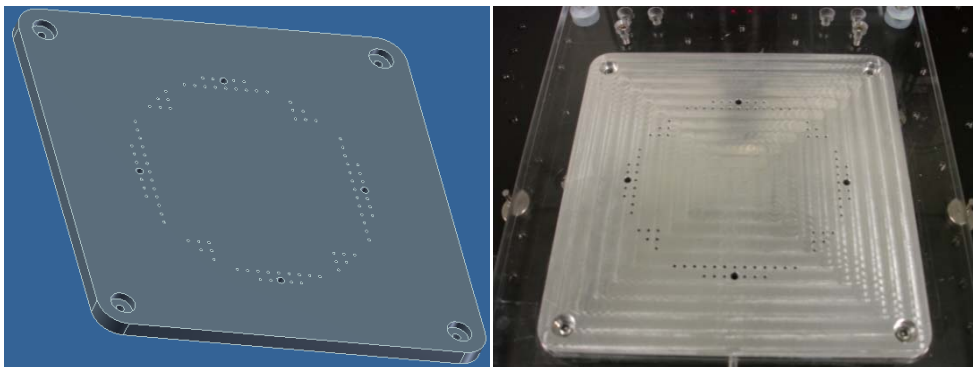


Figure 19 Screen printer substrate holder

The screen printer substrate holder design has been realized with the assistance of Dr Russel Torah and final manufacturing was done by the university of Southampton workshop department.

### III.III.II Device clamps

The university testing lab provided with a vibration generator (shaker) which was capable of creating the required vibrations for the chip devices. For each different device type a separate clamp design was manufactured to allow for positioning of the device on the shaker. In addition, the clamp was required to place each device as close as possible to the centre of the vibration generator. A Top plate drawing from Perpetuum Ltd, provided with the location of all available thread holes on the surface of the shaker [Appendix G].

The fact that all single cantilever devices were made with the same width, allowed for the design of a simple two piece clamp structure. The difference in length was compensated with the repositioning of the clamp on different shaker thread holes thus always maintaining the beam on the centre of the shaker.

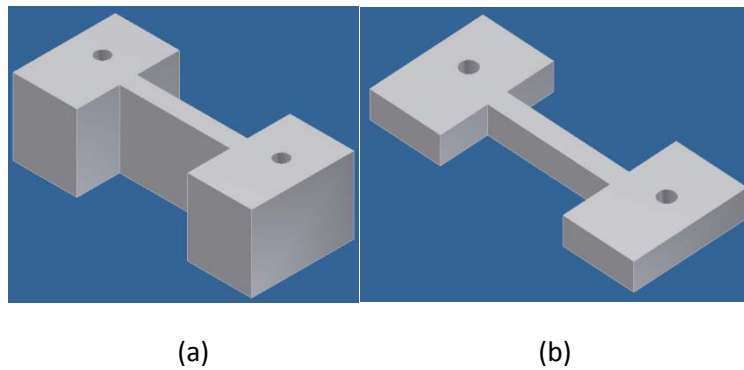


Figure 20 Single cantilever beam clamp: a) bottom piece, b) top piece

The three beam cantilever generator required a more complicated shaker clamp design since the beams were required to be free standing and positioned around the centre of the shaker. The clamp design consisted of three pieces. The bottom part ensured the connection of the clamp on the shaker rig while the two top pieces were holding the device in place.

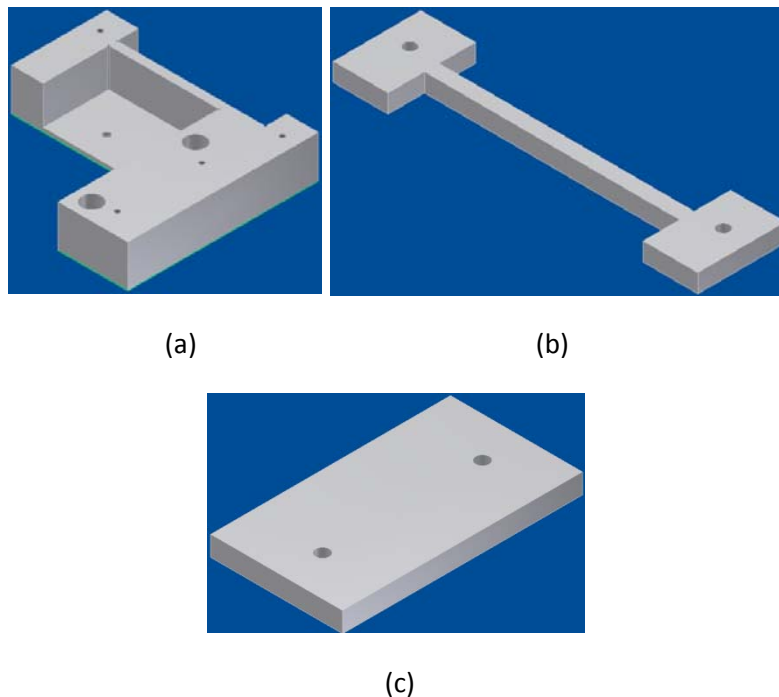
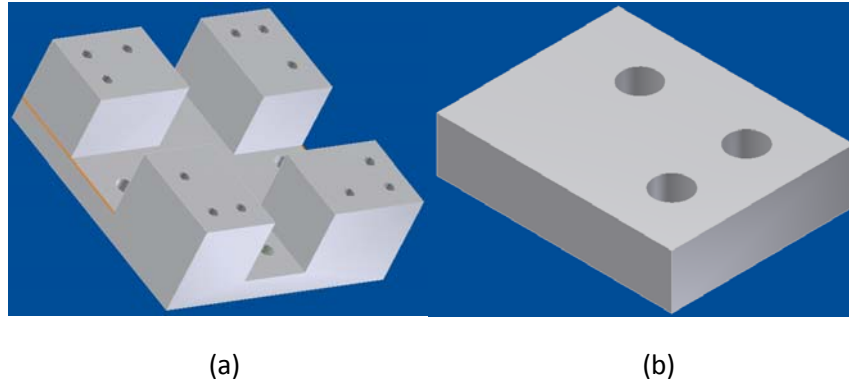


Figure 21 Three beam clamp design: a) bottom piece, b) and c) top pieces

Finally the Meandrical structure was required to have the central mass to be free standing so that it can deflect properly. Due to the square shape of the device the designed clamp placed a grip on the four corners of the chip. The clamp consisted of a bottom piece which connected with the shaker thread holes whereas four identical top pieces were securing the device in place.



**Figure 22 Meandrical device clamp design: a) bottom piece, b) top piece**

Detailed design dimensions are provided in Appendix H. Due to the lack of aluminium material with the specified thicknesses, all clamps were made out of tufet plastic. The device clamp inventor designs have been realized by Dr Russel Torah and Miss Charlene Nicoleau and final manufacturing was done by the University of Southampton workshop department. Autodesk inventor created files are included in Appendix CD.

## IV. Chapter 4 : Screen printing phase

### IV.I Screen printing ink preparation

As per discussed in section II.V, screen printing process relies on the deposition of different materials in the form of a paste. The paste can either be acquired directly from a supplier or it can be formulated with the use of a triple roll mill.

During formulation of the paste a series of ingredients are mixed together manually to form an unprocessed viscous liquid. Because of the nature of the manual mixing, the paste is required to become more homogeneous so that it can flow through the fine screen mesh without any material remaining on the screen. The triple roll mill consists of three rolls which rely on high pressure to squeeze large formed “lumps” of material so that they can be reduced to a smooth printable ink. The processed paste may be required to pass more than one time through the mill until the desired viscosity and homogeneity is reached.

### IV.II Mass ink

One of the novelties introduced in this project was the deposition of a thick film mass layer directly on the steel substrate. Since this method has not been tested in the past, a custom made ink was made by using the triple roll mill. The deposited material was selected to be tungsten and 1 $\mu$ m particle size and 4-6  $\mu$ m particle size tungsten powders were acquired from Ultimate Materials. The reason behind the acquisition of two different particle size powders was that large particles are able to form a strong bond when combined together inside a printed layer, however due to the non symmetrical particle shape, significant size gaps are created between the bonded particles which reduce the efficiency of the layer. The smaller particles are able to fill up the created gaps thus being able to have more material mass inside the printed layer.

In addition to the tungsten powder, a percentage of CF7575 lead borosilicate glass powder was added to the paste formulation. The glass was required for creating a solid bond with the tungsten during the firing process. Finally the different materials were mixed together with a V400 vehicle. Depending on the amount of inserted vehicle, the author was able to control the viscosity of the ink.

The basic tungsten ink formulation was based on a previously tested PZT formulation and consisted of a 32:68 mix of large particle size to small particle size powders from the remaining percentage of material after the introduction of glass. An initial attempt was made by combining different percentages of tungsten and glass and deposition on alumina substrates, in order to measure the resulting density. The different percentage values tested as part of this project were a tungsten mix of 10% glass, 20% glass, 30% glass and 60% glass. It is obvious that the higher the glass percentage the less the density of the resulting ink. From all printed inks, an acceptable result was only produced from the 60% glass formulation; however the resulting density was only 3360 kg/m<sup>3</sup>. For intermediate experimental results the reader is forwarded in Appendix I.

Since the resulting density was relatively low, an alternative approach was the combination of tungsten particles with ESL 240-SB polymer. Furthermore, the formulation of the mass ink was based on PZT principles where a high quality active material was required. However the tungsten layer would be used solely for creating a mass of the highest possible density. Therefore a second polymer formulation was composed by using polymer and 1  $\mu$ m tungsten particles only in an attempt to increase the density even further. For both polymer inks, density measurements were made on single printed substrates and double printed substrates.

For intermediate experimental results the reader is forwarded in Appendix I. The highest density was measured for the double print variable particle size tungsten ink which had a value of 7050kg/m<sup>3</sup>.

### IV.III Screen printer preparation

Prior to ink deposition each substrate needed to be setup with the screen printer. The substrate to be printed was placed on the substrate holder and was secured with four 3mm aluminium rods. The rods were mainly used to align the substrate to the substrate holder and were removed when the sample was ready to be inserted inside the printer.

As described in section III.II.II all screens contained a normal top down view of the devices and a mirror image. Since no printing could occur for both designs simultaneously, one of the two patterns had to be covered whilst the mirror design was being used by the printer. When all substrates were dried and fired or cured the screen was thoroughly cleaned, the last used pattern was covered and the mirror pattern was uncovered.

Whenever a new screen or mirror image of the same screen was used, the substrate was required to be aligned to the screen. This process involved the use of infrared cameras mounted on the screen printer which assisted the alignment process.



Figure 23 Thick film screen printer

As an initial step, the substrate to be aligned was covered with low residue tape and the substrate zero and print gaps were set through the printer set-up mode. Secondly the front and rear print limits on the screen were determined by scanning across the screen with the flood blade. Finally the screen was roughly aligned with the substrate through the screen apertures and a trial layer was deposited on the substrate. By using the cameras, the user could inspect the position of the deposited layer having as reference the substrate alignment aids. If required, the position of the substrate could be changed by using the x-axis, y-axis and  $\theta$ -axis angle knobs. The deposited layer was cleaned and after having changed the substrate position, new layers were deposited.

After achieving a perfect alignment, a reference image was captured through the cameras, which was used to align the next substrate directly, without having to perform the repetitive low residue tape process.



#### IV.IV Dielectric layer (ESL4924)

The dielectric layer was the first material to be deposited on the steel substrate. Since the author had no prior experience to alignment and precise positioning of the substrate, a decision was made to initiate printing using the three beam cantilever chip substrate. This decision was based on the fact that the design consisted of large surfaces and several 90 degree corners which resulted to an easier alignment compared to the individual chip design substrate.

Parameter	Value
Deposits	2
Forward Speed	70
Reverse Speed	60
Print Gap	1.5 mm
Front Print Limit	96 mm/180 mm (mirror design)
Rear Print Limit	231 mm/ 329 mm (mirror design)
Separation Speed	80%
Hop Over Distance	26 mm
Hop Over Delay	0 sec
Table in Delay	0 sec
Squeegee Delay	0
Inspection Rate	1
Alignment Rate	1
Pressure Setting	6.5 kg

Table 8 Dielectric printing profile

For simplicity reasons, during description of the printing process, the author refers to as “print”, the total number of dried layers of a single ink prior to firing or curing. A “deposit” is the total number of printing passes the squeegee performs on a single print.

For the dielectric layer, two prints of two deposits per print were deposited in order to account for any possible pin holes in the surface of the dielectric which could result to a short-circuit of the substrate with the bottom electrode. The dielectric was deposited and dried for both sides of the dielectric prior to firing since this approach would result to a minimum “deformation” of the steel due to thermal coefficient mismatching. The printed substrate was dried at an average of 140 °C. An example substrate was fired at an average temperature of 850 °C. The resulting total layer thickness, including the substrate thickness, was 237µm.

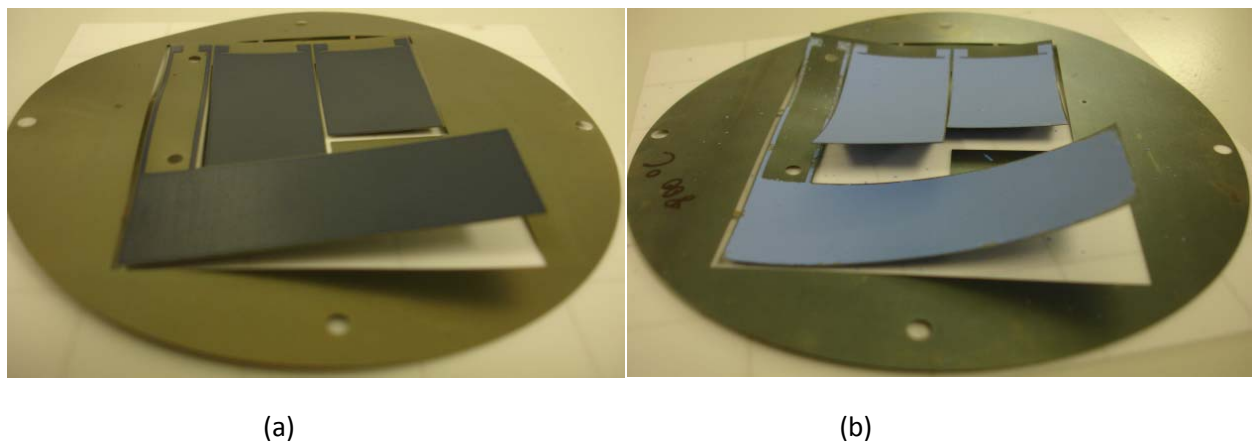


Figure 24 Three beam cantilever substrate. Fired dielectric layer at : a) 850 °C b) 800 °C



As it can be observed in figure 24 a) the firing process resulted to a severe deformation of the steel thus making any further deposition impossible. In order to reduce the deformation, a firing attempt on a second substrate was made at 800°C. Unfortunately the resulting layer was extremely brittle thus proving that the dielectric could not be fired at a lower temperature. Since the deformation would lead to a significant device performance reduction, a decision was made to halt the fabrication of the three beam cantilever substrate and proceed to the individual chip substrate.

During printing of the dielectric layer on the individual chip substrate the reverse speed was reduced to 35 in order to allow for deposition of material in sharp corners and small features on the substrate. Once more two prints of dielectric have been deposited on both sides of the substrate and fired at 850 °C.

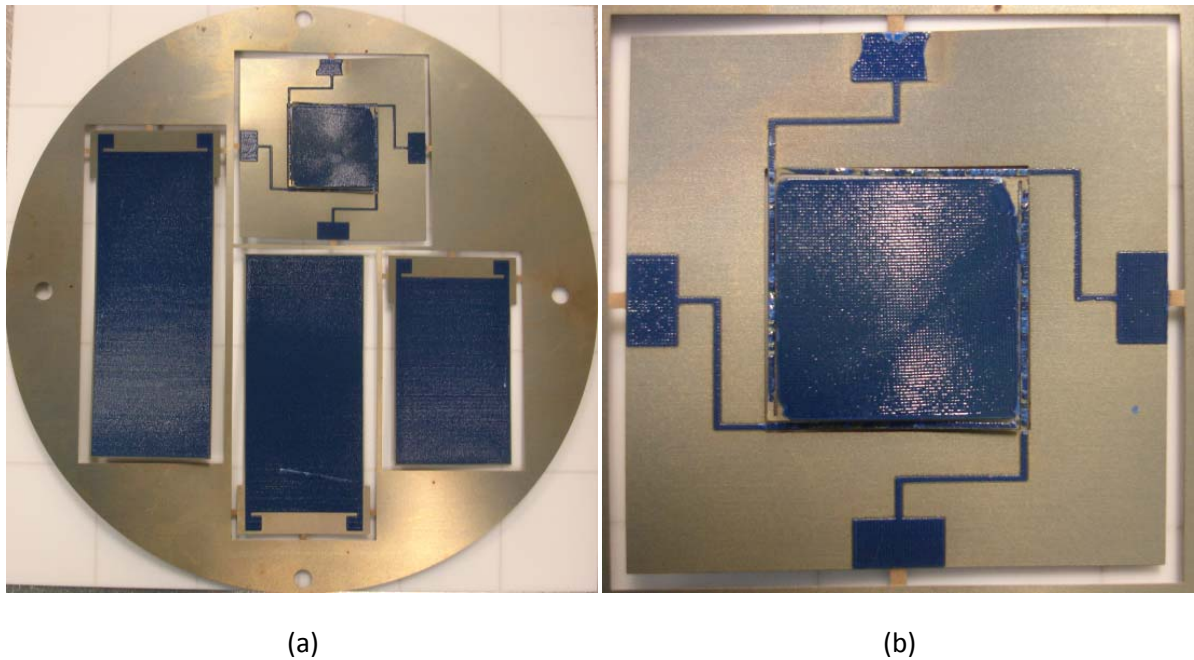
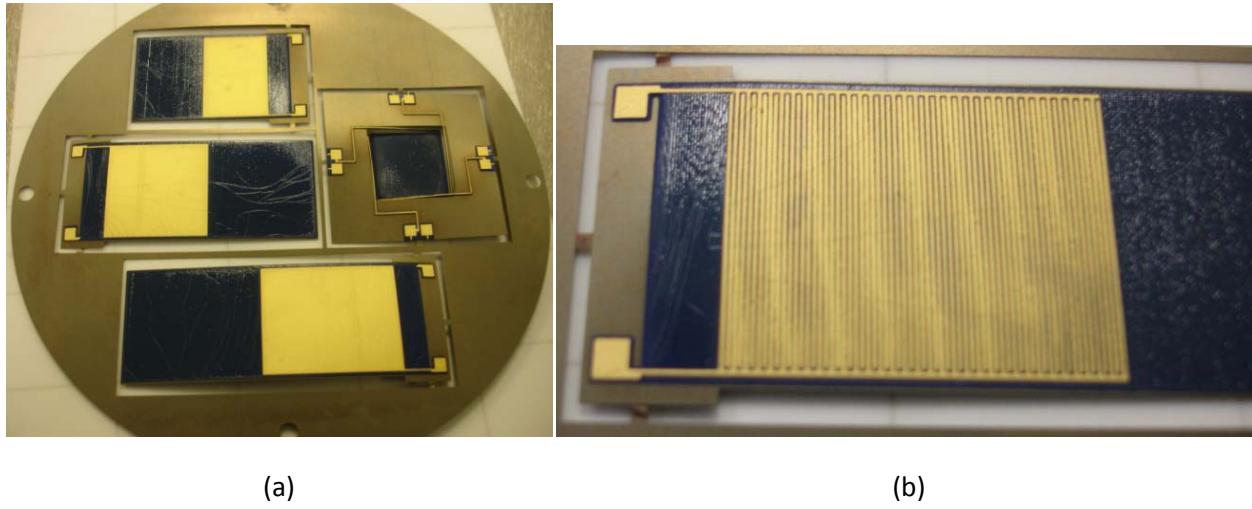


Figure 25 Individual chip substrate: a) Fired dielectric layer b) Zoom in on meandrical device

As it can be observed from figure 25, the resulting dielectric layer was satisfactory for all three cantilever beams with a small deformation occurring across the surface of the dielectric. The meandrical dielectric layer was completely damaged during the firing process. Due to the destruction caused by the firing process, two printed and dried dielectric deposited substrates were kept for co-firing. Such a process would allow for printing of all different materials prior to a single firing thus keeping the number of firing steps at minimum.

#### IV.V Bottom Electrode layer (ESL8836)

The ESL8836 gold ink is characterised by a high price and the ability to “bleed” easily after being deposited on the substrate. Therefore for the bottom electrode a single print of one deposit was more than adequate. The same printing profile as the dielectric layer was utilized with the exception of the deposits set to one. Once more the bottom electrode was dried at 140 °C for both sides and fired at 850 °C which resulted to a structure of 267µm total thickness. During the bottom electrode deposition four substrates were made with parallel electrodes (3 with fired dielectric substrates, 1 co-fired substrate), while 2 substrates were made with IDT 200µm electrodes (1 with fired dielectric substrate, 1 co-fired version).



**Figure 26 Bottom Electrode: a) Fired bottom electrode layer b) Zoom in of IDT electrodes**

As it can be observed from figure 26 a), the firing of the bottom electrode caused a cracking effect on the devices. Probing with a multimeter proved that there was no connectivity between the electrode and the substrate. Probing on the IDT devices revealed a short circuit between the two electrodes. This was caused from the bleeding nature of the golden ink (figure 26 b). No fabrication was attempted with the 150 $\mu$ m screen since it would result to an even worse bleeding effect. Probing on the co-fired IDT devices revealed no short circuit thus fabrication was continued for this substrate.

#### IV.VI PZT layer (PZT-5H)

The PZT layer was the third layer deposited on the devices. For the PZT layer two prints were made in order to avoid any short circuits between the top and bottom electrode; however since ANSYS simulated PZT thickness was 50 $\mu$ m, the first print was made with two deposits while the second print with only one deposit to avoid the creation of a very thick PZT layer. Once more the dielectric print profile was used with the exception of the deposits number. The PZT was dried at 140 °C for both sides and both prints and fired at 850 °C which resulted to a structure of 407 $\mu$ m total thickness.

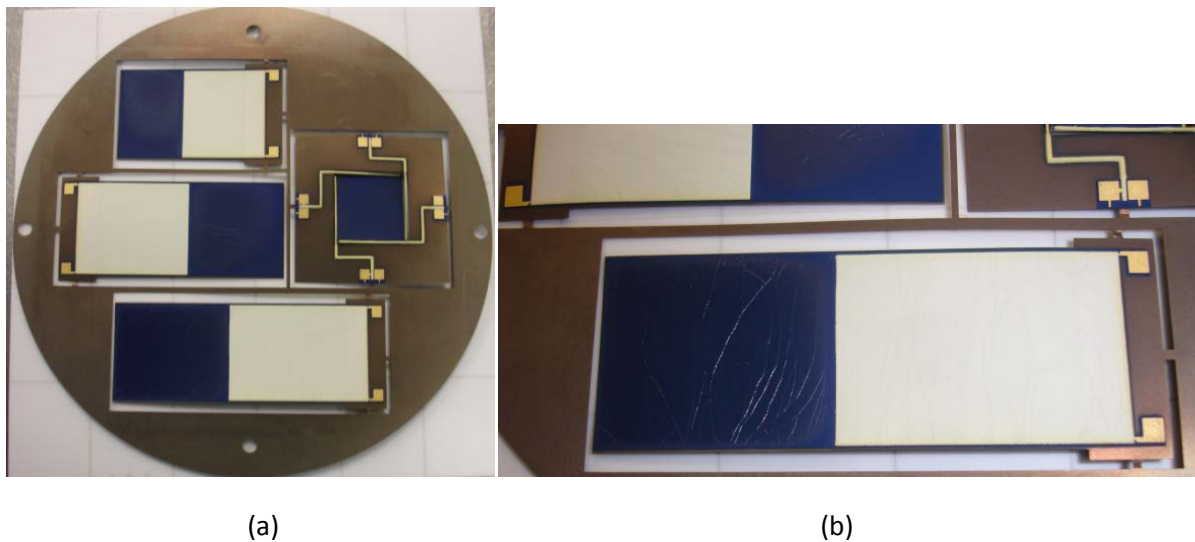


**Figure 27 a) Fired PZT layer b) Zoom in on PZT layer**

Close inspection of the fired PZT layer revealed the same cracking effect which occurred on the dielectric and bottom electrode layers. The PZT layer was the final layer for the IDT co-fired devices that required firing; henceforth the substrate was fired at 850 °C.

#### IV.VII Top electrode layer (ESL1901-S)

In order to avoid further deterioration of the device due to thermal stresses while firing, a decision was made to deposit a conductive polymer top electrode instead of gold. The advantage of using a polymer ink was that it involved only a curing process at 125 °C instead of firing at 850 °C. The disadvantage of the polymer ink was that it was polymerizing rapidly with air thus turning into solid during printing. This condition led to further re-alignment of the screen to the printer since the screen had to be removed and thoroughly cleaned before re-initiating printing.

Similar to the golden bottom electrode ink, the silver conductive polymer was flowing easily on the surface of the device after deposition. Therefore only one print was performed with three depositions. Despite the fact that three ink depositions were quite a lot for a conductive polymer, they were required in order to successfully connect the top electrode area with the electrode pad. The layer was cured at 125 °C for both sides and resulted to a total device thickness of 447µm.

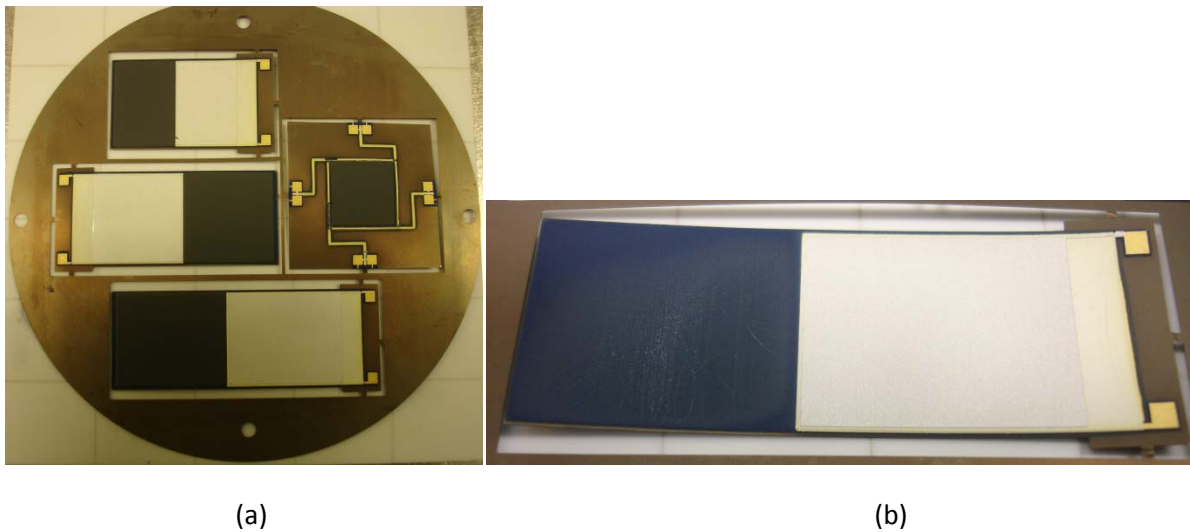


Figure 28 a) Cured top electrode layer b) Zoom in on top electrode layer

Probing on the top electrode area and the top electrode pad proved that a successful connection has been achieved over the PZT step. Further probing on the bottom and top electrode pads revealed a short circuit between the two layers in all the devices. Since this problem could be further investigated during testing of the devices, a decision was made to finalize the manufacturing process by placing the final mass layer.

#### IV.VIII Mass layer (custom made polymer tungsten ink)

The mass layer was the final layer to be printed on the devices. As per described in section IV.II, the mass ink consisted of a polymer based ink therefore only drying and curing was required to create a solid mass volume. The process for printing the mass on the devices consisted of multiple deposits and dries at 140 °C until a thickness of approximately 200µm was achieved for both sides. Such a thickness required three prints of two deposits on the substrate. A final curing at 215 °C ensured the solidification of the mass. During printing of the mass layer a decision was made to not deposit mass on one substrate. This decision was based on the fact that although the devices were perfectly simulated to have specific resonant frequencies, due to the nature of the screen printing process, the resulting layer thicknesses were not similar to the simulated model thus changing the frequency of the device. By not including a mass layer, the resonant frequency could be fine tuned by attaching a weighted mass during the testing phase.

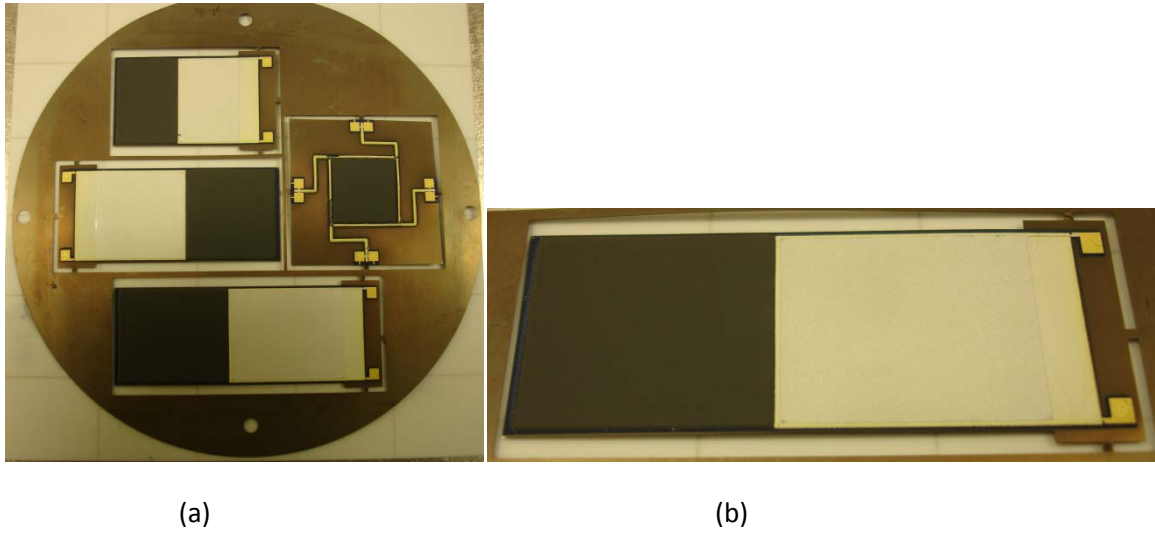


Figure 29 a) Cured mass layer b) Zoom in on mass layer

The resulting overall thickness measured on the mass area was 650  $\mu\text{m}$ , including the dielectric and the steel substrate thickness. Weight measurement of the devices with and without mass allowed for a more accurate tungsten density calculation.

Device type	Device weight without mass (kg)	Device weight with mass (kg)	Mass volume ( $\text{m}^3$ )	Density ( $\text{kg}/\text{m}^3$ )
30Hz cantilever	$1.63 \times 10^{-3}$	$3.33 \times 10^{-3}$	$170.62 \times 10^{-9}$	9963.66
45Hz cantilever	$1.38 \times 10^{-3}$	$2.87 \times 10^{-3}$	$142.88 \times 10^{-9}$	10428
93Hz cantilever	$1.06 \times 10^{-3}$	$2.04 \times 10^{-3}$	$98.80 \times 10^{-9}$	9919

Table 9 Cantilever beam calculated mass density

## V. Chapter 5: Testing

### V.I Polarisation

Polarisation of the PZT layer was achieved by applying an electric field on the two electrodes whilst the device was under increased temperature. During polarisation it was essential to polarize both sides of the device since a second attempt to increase the temperature without applying an electric field would depolarize either side. In order to achieve the same poling direction for both PZT layers, the top electrode of one side was wired together with the bottom electrode of the opposite side and vice versa.

Prior to application of the electric field, a voltage of 240V – 400V was applied to the bottom and top electrode in order to “burn” the short circuit and electrically isolate the two electrodes. In certain occasions the damage was unreparable. Close inspection on the surface of the devices revealed that major damage occurred along the lines formed from the cracking effect. This condition led to a dramatic reduction of the devices performance since the PZT layer was significantly damaged.

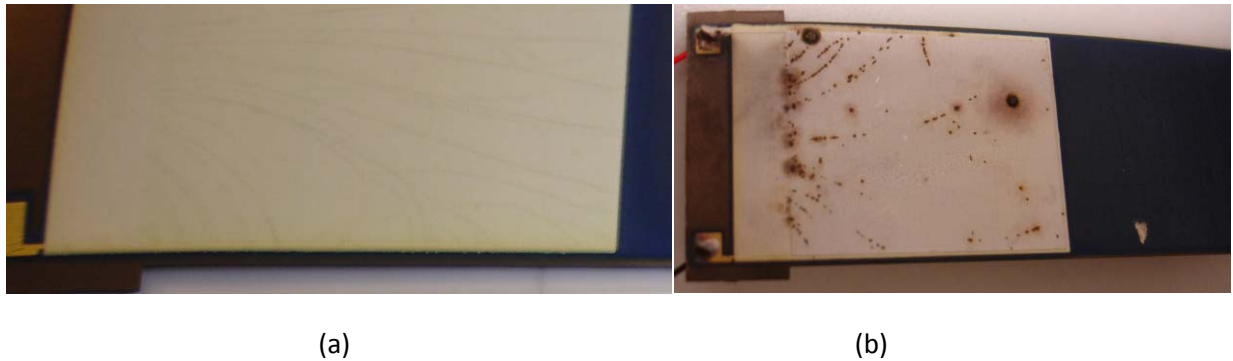


Figure 30 a) PZT layer cracking effect after firing b) Destroyed short circuits on the top electrode surface

For polarization, an electric field of  $4\text{MVm}^{-1}$  was applied and the samples were heated at  $200^\circ\text{C}$ . The field was maintained for 50 minutes allowing for 30 minutes at high temperature and 20 minutes for cool down.

### V.II Vibration generator testing

In order to test each individual cantilever beam, the device was secured on the custom made testing clamp and on to the vibration generator aluminium plate.

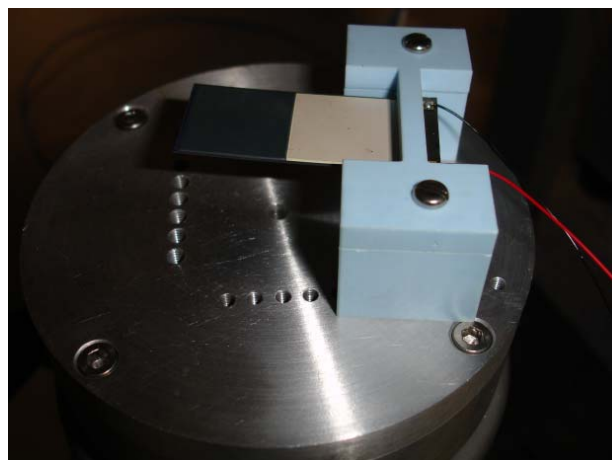


Figure 31 Mounted cantilever beam generator



With the assistance of LabView simulation software, the operator was able to inspect the performance of the device by applying different resistance loads, amplitude and frequency of vibration. Furthermore a series of steps could be programmed as an input file in order to allow multiple simulations to be run automatically. The results were collected from an output file and presented in a graphical form.

In figure 32 it is possible to observe the performance of a designed 45Hz cantilever beam generator. Results were taken from only one side of the device thus the power output can be potentially doubled.

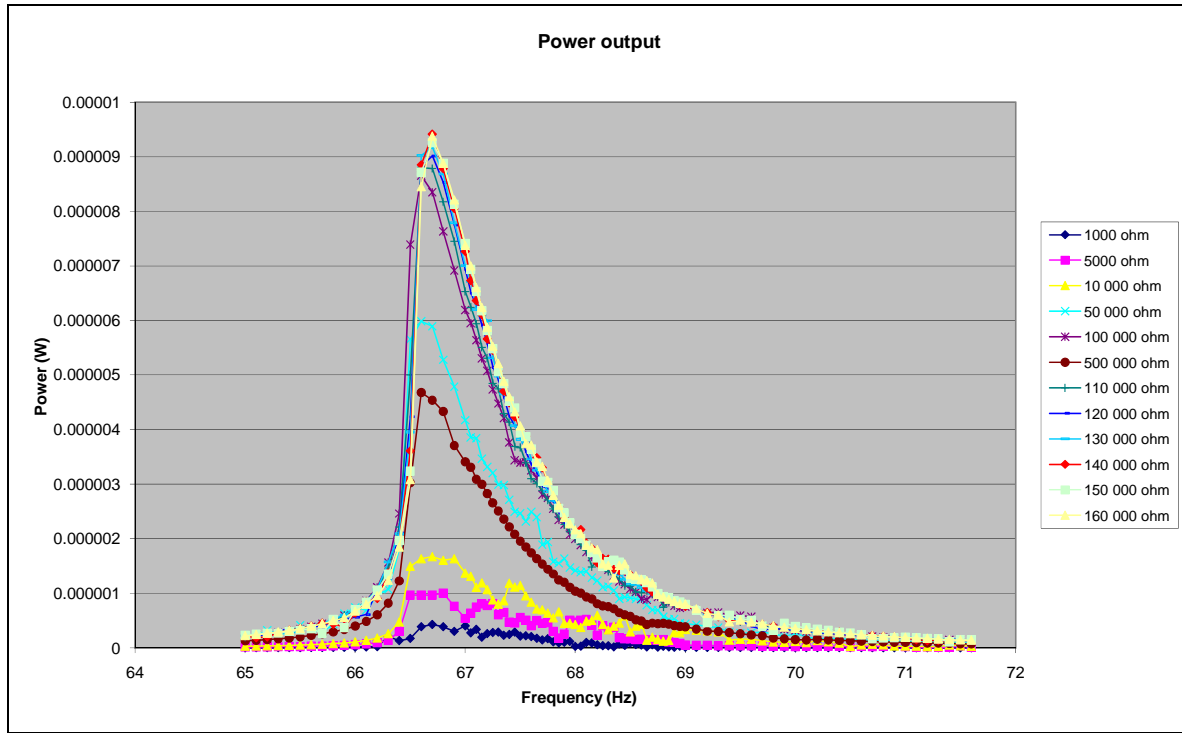


Figure 32 Power output for a 45Hz cantilever beam for variable resistance at 100mG acceleration

Maximum power output of  $9.37\mu\text{W}$  was being produced at an optimum load resistance of 140k ohm. It is also possible to observe that the resonant frequency of the device was situated at 66.7Hz. Such a difference between the simulated 45Hz frequency and the actual resonant frequency can be expected due to the nature of screen printing which created different layer thicknesses compared to all ANSYS simulated layers. Further increase in power can be achieved by increasing the level of acceleration.

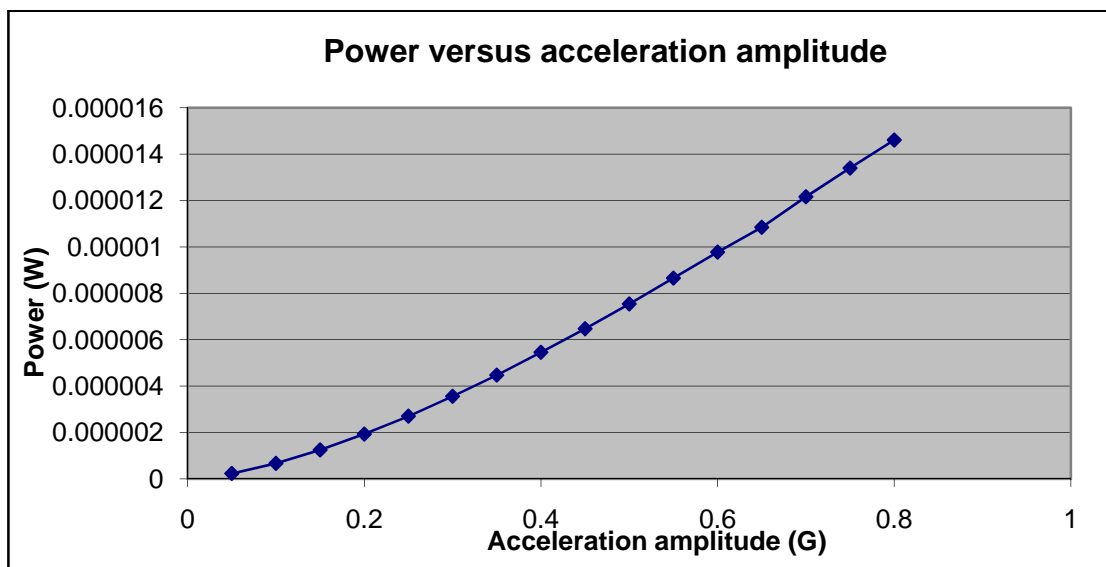


Figure 33 Increased power output at increased acceleration under optimum load resistance and resonant frequency

A comparison between figure 32 and 33 reveals a conflict of power output values at 100mG acceleration. This difference can be explained due to fatigue of the device occurring during testing. Furthermore, constrained stresses within the different device layers were being released while the device was under displacement. An interesting inspection was that any increase of acceleration resulted to a change of resonant frequency.

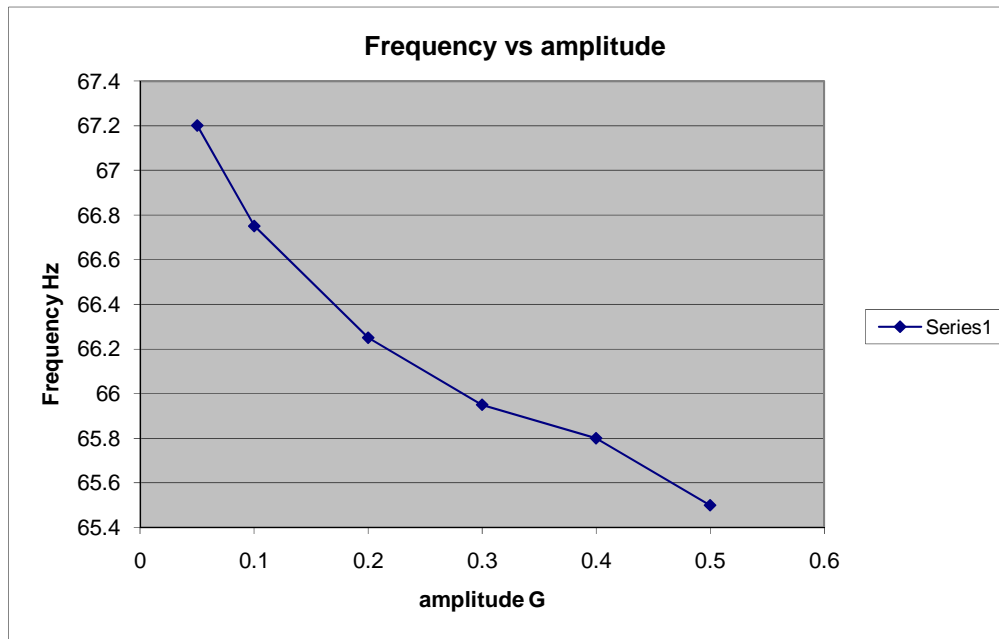


Figure 34 Reduction of resonant frequency due to increased acceleration

Finally, a maximum open loop output power of  $0.56\mu\text{W}$  was measured by connecting the device to a 5M ohm load resistance.

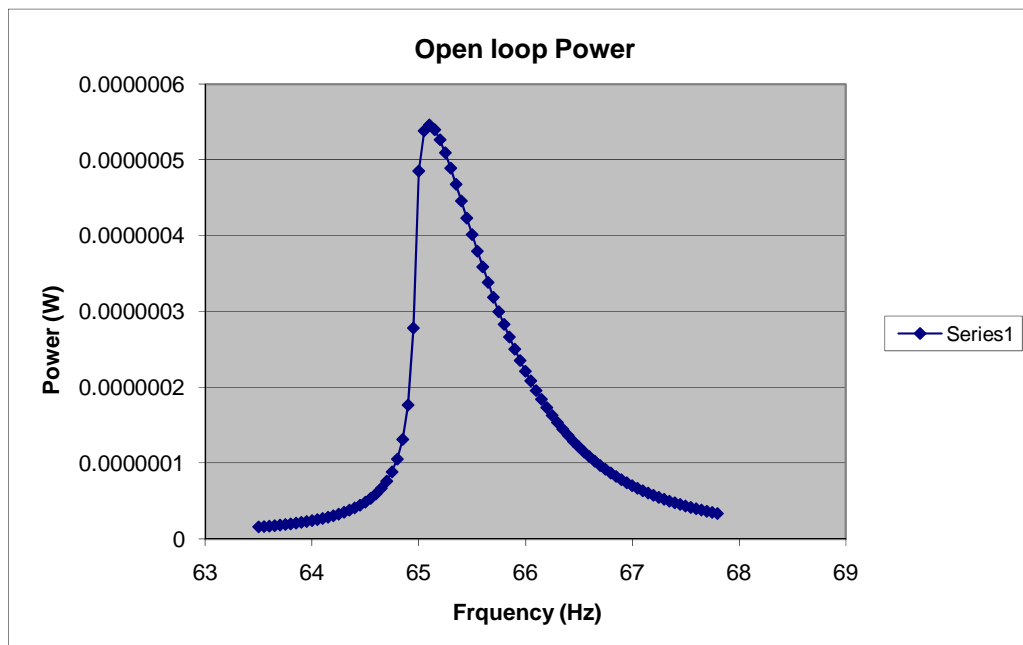


Figure 35 Open loop output power at 100mG acceleration

The difference between theoretically calculated output power, as presented in appendix E, and actual output power can only be explained due to the damage of the PZT layer during repairing of device short circuits and the difference in layer thicknesses. For detailed device experimental results the reader is forwarded to appendix J.

Tested device	Tested resonant frequency at 100mG (Hz)	Output power at 100mG (W)	Optimum load (Ohm)	Open loop power (W)	Open loop voltage (V)
45Hz cantilever with tungsten mass	66.7	$9.37 \times 10^{-6}$	$140 \times 10^3$	$0.56 \times 10^{-6}$	1.6
45Hz co fired cantilever IDT with tungsten mass	65.8	$0.49 \times 10^{-6}$	$900 \times 10^3$	$2.18 \times 10^{-8}$	0.44
30Hz cantilever with tungsten mass	59.05	$6.04 \times 10^{-6}$	$80 \times 10^3$	$7.3 \times 10^{-8}$	0.6
30Hz cantilever with 1.62g glued mass	30.1	$6.48 \times 10^{-7}$	$200 \times 10^3$	$1.98 \times 10^{-8}$	0.31

Table 10 Experimental results from different piezoelectric generators



## VI. Chapter 6: Cost and time analysis

### VI.I Cost analysis

All practical work which contributed towards the completion of the piezoelectric devices had an associated cost.

Item	Cost (GBP)
Thick film screens (14 screens)	980
430s17 Stainless steel substrates (2 designs x 10 substrates)	400
S.E.M. equipment usage slot	75
Tungsten powders (500g)	160
Golden conductor Paste ESL8836 (3.6g)	15.7
Silver polymer paste ESL1901-S (1.8g)	2.55
Overglaze dielectric polymer paste ESL4924 (14.4g)	30
PZT-5H piezoelectric material (7.2g)	14.4
<b>Total Cost</b>	<b>1677.65</b>

Table 11 Piezoelectric generators associated cost

By observing table 11, it is noticeable that the highest cost consists of the thick film screens. Despite the overall cost figure, it is important to consider that the screens can still be reused at future printing designs thus eliminating this figure from future project budgets. The S.E.M. equipment usage cost was a necessity towards detailed documentation of the novel tungsten printed ink. Finally all remaining costs were created during screen printing of the devices and should be considered as consumable costs.

### VI.II Time analysis

The completion of all design work, practical work and creation of this document spanned through a fifteen week period. In order to plan and monitor the progress of the MSc project, a Gant chart was created which included all steps from initial background research up to the handing of the written thesis. In table 12, it is possible to compare the planned progress with the actual progress.

Week (starting week beginning 9 <sup>th</sup> June)	1	2	3	4	5	6	7	8	9	10	11	12	13	14	15
<b>Activities and milestones</b>															
Background research															
Literature review															
ANSYS research, device architecture design															
Architecture simulation															
Substrate mask design and external manufacturing (2 weeks EDT*)															
Milestone - finish substrate design															
Material layer screen design and external manufacturing (2 weeks EDT)															
ANSYS electrical potential simulation															



## **VII. Chapter 7: Conclusion and suggestions for further work**

### **VII.I Suggestions for further work**

During manufacturing of the piezoelectric generators a cracking effect appeared on the surface of the dielectric insulating layer upon firing of the devices. Connectivity probing revealed no short circuit between the bottom electrode and the substrate thus leading the author to believe that this condition was only a surface effect without any impact on the device performance. However during testing, the destroyed areas on the device surface revealed that this effect caused the short circuit of the top and bottom electrode thus significantly reducing the device performance. Discussion with academic staff determined that the source of this effect was the initial deformation of the steel substrate under high temperatures. In the event of future substrate design reconsideration, the author would recommend the increase of steel substrate thickness in order to allow for less deformation. Such an approach should be re simulated in all ANSYS device models, to determine the impact on the device resonant frequency. Furthermore additional separation tags should be included around the devices in order to further decrease deformation.

All screens created for this project contained relatively large area designs next to small areas. A typical example was the meandrical structure cantilever beams which were placed next to large areas. Such a design required multiple depositions since the material was not being easily deposited due to the complexity of the design. A possible approach would be to decrease the ratio between disproportional areas. Further increase of the dimensions of the meandrical beams could also eliminate the extreme deformation of this device during firing.

Finally, as per described in chapter two of this document, produced energy from a piezoelectric generator could be potentially stored in a capacitive structure. The creation of such a structure could be combined with the already developed generators in order satisfy the energy storage requirement of the EU TRIADE project. The interconnection of the two elements could be achieved with an electronic interface circuit.

### **VII.II Conclusion**

Within this document, the author presented a successful production of a series of custom designed piezoelectric generators. Overall the MSc thesis project was delivered on time, as per inspected from section VI.II, with a satisfactory output power of  $9.3\mu\text{W}$  at  $100\text{mG}$  acceleration. Despite the fact that the produced output power was significantly lower compared to the theoretical calculated power, the level of achieved output power, at high acceleration values, is still usable for a variety of sensing sensors. Further ANSYS simulations could be performed by replacing the simulated layer thicknesses with the actual achieved thick film printed thicknesses and the simulated material properties with the various ink properties. Such a simulation would then provide with new resonant frequency and output power values which could be compared with the tested results.

Overall this project has greatly enhanced the authors design skills, since it provided an opportunity to investigate software design packages such as ANSYS, L-edit and Autodesk inventor. ANSYS introduced the previously unknown, finite element analysis theory and the different methods it can be implemented for successful design of a solid structure.

This MSc project has also provided the opportunity to the student to involve himself in different areas such as design, simulation and practical fabrication thus maintaining a constant interest throughout a four month period. The use of thick film process equipment was definitely an advantage towards the student's future professional carrier. Finally, in addition to the successful delivery of a finalized project, all associated results will be written in an academic paper and presented to the Power MEMS 2008 conference.

## VIII. Appendices

### Appendix A: Cantilever beam theoretical resonant frequency calculation

Resonant frequency can be calculated by using the formula:

$$f_n = \frac{(k_n l)^2}{2\pi l^2} \left( \frac{\int_h E(z - z_0)^2 dz}{\sum_{i=1}^N (h_i \rho_i)} \right)^{\frac{1}{2}}$$

Where  $k$  = modal parameter,  $l$  = length of cantilever,  $h$  = thickness of layer,  $\rho$  = density of material and  $E$  = young's modulus [34]

For a simple cantilever structure of one steel substrate, two dielectric layers, two PZT layers and two electrode layers the equation can be calculated as follows:

Layer	Young's modulus (Pa)	Density (Kg/m <sup>3</sup> )	Thickness (μm)
Stainless steel substrate	$E_s = 2 \times 10^{11}$	$\rho_s = 7750$	$T_s = 100$
Pyrex dielectric layer	$E_d = 6.4 \times 10^{10}$	$\rho_d = 2230$	$T_d = 20$
Golden electrode layer	$E_e = 8 \times 10^{10}$	$\rho_e = 19280$	$T_e = 10$
PZT active layer	$E_{PZT} = 15 \times 10^9$	$\rho_{PZT} = 7750$	$T_{PZT} = 50$

Table 13 Theoretical cantilever structure layer parameters

$$\sum_{i=1}^5 (h_i \rho_i) = T_s \rho_s + 2x T_d \rho_d + 2x T_{PZT} \rho_{PZT} + 2x T_e \rho_e \quad (1)$$

$$\begin{aligned} \int_h E(z - z_0)^2 dz &= \int_0^{T_{PZT}} E_{PZT}(z - z_0)^2 dz + \int_{T_{PZT}}^{T_{PZT}+T_e} E_e(z - z_0)^2 dz \\ &+ \int_{T_{PZT}+T_e}^{T_{PZT}+T_e+T_d} E_d(z - z_0)^2 dz + \int_{T_{PZT}+T_e+T_d}^{T_{PZT}+T_e+T_d+T_s} E_s(z - z_0)^2 dz \\ &+ \int_{T_{PZT}+T_e+T_d+T_s}^{T_{PZT}+T_e+T_d+T_s+T_d} E_d(z - z_0)^2 dz + \int_{T_{PZT}+T_e+T_d+T_s+T_d}^{T_{PZT}+T_e+T_d+T_s+T_d+T_e} E_e(z - z_0)^2 dz \\ &+ \int_{T_{PZT}+T_e+T_d+T_s+T_d+T_e}^{T_{PZT}+T_e+T_d+T_s+T_d+T_e+T_{PZT}} E_{PZT}(z - z_0)^2 dz \quad (2) \end{aligned}$$

For a cantilever beam of  $l = 50\text{mm}$ :  $k_n l \approx 1.8751, 4.6941, 7.8548, 10.9955, 14.1372$  for the first five modes of operation.

Based on first mode of operation  $k_1 l = 1.8751$  and equation (1) and (2)

$$f_n = \frac{(k_n l)^2}{2\pi l^2} \left( \frac{\int_h E(z - z_0)^2 dz}{\sum_{i=1}^N (h_i \rho_i)} \right)^{\frac{1}{2}} = 83.78 \text{ Hz}$$

For a structure with more layers, further additions and integrations of equation (1) and (2) are required to consider the total structure.

This theoretical analysis was provided by Miss Charlene Nicoleau, University of Southampton student.

## Appendix B: Validation of theoretical, SOLID 45 and SHELL 99 structure results for meshing grade finalization

In section III.I.II, the author analysed the necessity of performing mapped meshing by specifying the element division for every created volume line. Such a division could be performed by selecting all lines of specific length and specifying manually the number of elements. Originally the element count was one element per 1mm for every line. For the Z plane, a maximum number of three elements was selected. Experimental simulations were performed in order to determine if further refinement of the meshing was required. Initially a simulation with only top and bottom dielectric layers, electrodes and PZT layers was performed with a 50 $\mu$ m thickness substrate. From table 14 it is possible to observe that the three models produced almost identical values. Further refinement of the meshing by dividing lines into more elements had no change to the experimental results.

Further simulations were performed by adding more layers, changing the dimensions of the device and also, only for model validation purposes, changing the Young's modulus values for different materials, and observing the impact on the produced frequency. Unfortunately though, the theoretical frequency produced from the equation in Appendix A, was unable to provide with correct results when the mass layer was added to the structure. Despite this obstacle the meshing grade was successfully determined and simulations could be performed with the Solid 45 and Shell 99 models to finalize the device dimensions.

Design Parameters	Theoretical frequency (Hz)	Solid 45 frequency (Hz)	Shell 99 frequency (Hz)
with steel 50 + 2diel 20+2el10+PZt50	26.1	26.9	26.9
with steel 50 + 2diel 20+2el10+PZt50 finer meshing	26.1	26.9	26.9
with steel 50 + 2diel 20+PZt50	25.2	25.8	25.8
with steel 50 + 2diel 20+2el10+PZt50 Epzt=15e11	188.9	193.3	192.9
with steel 50 + 2diel 20+4el10+PZt50 Epzt=15e9	32.9	34.2	34
with steel 50 + 2diel 20+4el10+PZt50 Epzt=15e9 W=4cm increase	32.9	33.8	34.6
with steel 50 + 2diel 20+4el10+PZt50 Epzt=15e9 W=1cm decrease	32.9	35.5	33.6
with steel 50 + 2diel 20+4el10+PZt50 Epzt=15e9 L=70cm increase	16.8	17.4	17.2
with steel 50 + 2diel 20+4el10+PZt50 Epzt=15e9 L=30cm decrease	91.3	96.2	95.6
with steel 50 + 2diel 20+4el10+PZt50 Epzt=15e9 T=50 (substrate thickness=100) increase	43.2	44.6	44.5
with steel 50 + 2diel 20+4el10+PZt50 Epzt=15e9 Es=3e11 increase	33.3	34.7	34.5
with steel 50 + 2diel 20+4el10+PZt50 Epzt=15e9 Es=1e11 decrease	32.4	33.8	33.6
with steel 50 + 2diel 20+4el10+PZt50 Epzt=15e9 Ed=3e11 increase	37.6	38.9	38.8
with steel 50 + 2diel 20+4el10+PZt50 Epzt=15e9 Ed=0,64e10 decrease	31.6	33	32.8
with steel 50 + 2diel 20+4el10+PZt50 Epzt=15e9 Ee=2e11 increase	45.4	47.5	47.2

Table 14 Experimental validation of theoretical, solid 45 and shell 99 frequency values

Experimental results produced by collaboration of the author with Miss Charlene Nicoleau, University of Southampton student.

## Appendix C: Validation of SOLID 45 and SHELL 99 structure results for dimensions finalization

By using Solid 45 and Shell 99 models, it was possible to determine the final device dimensions. Simulations were performed by varying the substrate and mass thicknesses and observing the impact to the frequency. Furthermore a second set of variables was the length and width of the device and their impact to the frequency.

Beam Device		
	Shell 99 model (Hz)	Solid 45 model (Hz)
Default Device, 50 $\mu$ m sub+2diel 20 $\mu$ m+4*elec 10 $\mu$ m+2*PZT 50 $\mu$ m+2*mass 70 $\mu$ m W = 2cm, L = 5cm, Lm = 2/5*L	29.30	29.50
sub = 100 $\mu$ m, mass = 100 $\mu$ m	34.70	35.00
sub = 100 $\mu$ m, mass = 150 $\mu$ m	29.70	30.00
sub = 100 $\mu$ m, mass = 200 $\mu$ m	26.40	26.70
sub = 150 $\mu$ m, mass = 100 $\mu$ m	45.90	46.20
sub = 150 $\mu$ m, mass = 150 $\mu$ m	39.80	40.10
sub = 150 $\mu$ m, mass = 200 $\mu$ m	35.70	35.90
sub = 200 $\mu$ m, mass = 100 $\mu$ m	58.30	58.60
sub = 200 $\mu$ m, mass = 150 $\mu$ m	51.20	51.50
sub = 200 $\mu$ m, mass = 200 $\mu$ m	46.10	46.50

Beam Device	Shell 99 model (Hz)	Solid 45 model (Hz)
sub = 100 $\mu$ m, mass = 100 $\mu$ m,L=4cm	54.60	55.00
sub = 100 $\mu$ m, mass = 150 $\mu$ m,L=4cm	46.80	47.20
sub = 100 $\mu$ m, mass = 200 $\mu$ m,L=4cm	41.50	42.00
sub = 150 $\mu$ m, mass = 100 $\mu$ m,L=4cm	72.00	72.50
sub = 150 $\mu$ m, mass = 150 $\mu$ m,L=4cm	62.50	63.00
sub = 150 $\mu$ m, mass = 200 $\mu$ m,L=4cm	55.90	56.50
sub = 200 $\mu$ m, mass = 100 $\mu$ m,L=4cm	91.50	92.00
sub = 200 $\mu$ m, mass = 150 $\mu$ m,L=4cm	80.30	80.90
sub = 200 $\mu$ m, mass = 200 $\mu$ m,L=4cm	72.40	72.90

Beam Device	Shell 99 model (Hz)	Solid 45 model (Hz)
sub = 100 $\mu$ m, mass = 100 $\mu$ m,W=5cm,L=4cm	55.40	55.80
sub = 100 $\mu$ m, mass = 150 $\mu$ m,W=5cm,L=4cm	47.50	47.80
sub = 100 $\mu$ m, mass = 200 $\mu$ m,W=5cm,L=4cm	42.20	42.60
sub = 150 $\mu$ m, mass = 100 $\mu$ m,W=5cm,L=4cm	72.90	73.40
sub = 150 $\mu$ m, mass = 150 $\mu$ m,W=5cm,L=4cm	63.30	63.80
sub = 150 $\mu$ m, mass = 200 $\mu$ m,W=5cm,L=4cm	56.70	57.20
sub = 200 $\mu$ m, mass = 100 $\mu$ m,W=5cm,L=4cm	92.60	93.10
sub = 200 $\mu$ m, mass = 150 $\mu$ m,W=5cm,L=4cm	81.20	81.70
sub = 200 $\mu$ m, mass = 200 $\mu$ m,W=5cm,L=4cm	73.20	73.80

Beam Device	Shell 99 model (Hz)	Solid 45 model (Hz)
sub = 100 $\mu$ m, mass = 100 $\mu$ m,W=1cm,L=5cm	34.30	34.40
sub = 100 $\mu$ m, mass = 150 $\mu$ m,W=1cm,L=5cm	29.40	29.50
sub = 100 $\mu$ m, mass = 200 $\mu$ m,W=1cm,L=5cm	26.10	26.30

sub = 150μm, mass = 100μm,W=1cm,L=5cm	45.30	45.50
sub = 150μm, mass = 150μm,W=1cm,L=5cm	39.30	39.60
sub = 150μm, mass = 200μm,W=1cm,L=5cm	35.20	35.40
sub = 200μm, mass = 100μm,W=1cm,L=5cm	57.70	57.90
sub = 200μm, mass = 150μm,W=1cm,L=5cm	50.60	50.80
sub = 200μm, mass = 200μm,W=1cm,L=5cm	45.60	45.90

Beam Device	Shell 99 model (Hz)	Solid 45 model (Hz)
sub = 100μm, mass = 100μm,W=2cm,L=3cm	97.60	98.30
sub = 100μm, mass = 150μm,W=2cm,L=3cm	83.60	84.30
sub = 100μm, mass = 200μm,W=2cm,L=3cm	74.30	75.00
sub = 150μm, mass = 100μm,W=2cm,L=3cm	128.70	129.50
sub = 150μm, mass = 150μm,W=2cm,L=3cm	111.70	112.50
sub = 150μm, mass = 200μm,W=2cm,L=3cm	100.00	100.90
sub = 200μm, mass = 100μm,W=2cm,L=3cm	163.40	164.30
sub = 200μm, mass = 150μm,W=2cm,L=3cm	143.40	144.40
sub = 200μm, mass = 200μm,W=2cm,L=3cm	129.30	130.30

Beam Device	Shell 99 model (Hz)	Solid 45 model (Hz)
sub = 100μm, mass = 100μm,W=5cm,L=3cm	98.70	99.60
sub = 100μm, mass = 150μm,W=5cm,L=3cm	84.60	85.40
sub = 100μm, mass = 200μm,W=5cm,L=3cm	75.20	76.00
sub = 150μm, mass = 100μm,W=5cm,L=3cm	130.00	131.00
sub = 150μm, mass = 150μm,W=5cm,L=3cm	112.80	113.80
sub = 150μm, mass = 200μm,W=5cm,L=3cm	101.00	102.00
sub = 200μm, mass = 100μm,W=5cm,L=3cm	165.00	166.00
sub = 200μm, mass = 150μm,W=5cm,L=3cm	144.70	145.90
sub = 200μm, mass = 200μm,W=5cm,L=3cm	130.50	131.60

Beam Device	Shell 99 model (Hz)	Solid 45 model (Hz)
sub = 100μm, mass = 100μm,W=5cm,L=5cm	35.30	35.60
sub = 100μm, mass = 150μm,W=5cm,L=5cm	30.30	30.50
sub = 100μm, mass = 200μm,W=5cm,L=5cm	26.90	27.10
sub = 150μm, mass = 100μm,W=5cm,L=5cm	46.60	46.80
sub = 150μm, mass = 150μm,W=5cm,L=5cm	40.40	40.70
sub = 150μm, mass = 200μm,W=5cm,L=5cm	36.20	36.40
sub = 200μm, mass = 100μm,W=5cm,L=5cm	59.10	59.40
sub = 200μm, mass = 150μm,W=5cm,L=5cm	51.90	52.10
sub = 200μm, mass = 200μm,W=5cm,L=5cm	46.80	47.10

Table 15 Modified dimensions experimental results

Since all three different devices were required to have the same substrate and mass thicknesses, a decision was required that would allow for only slight length and width variations for reaching the target frequency. However a decision was made to maintain the width of all devices the same since such an approach would have an impact to the device testing equipment design.

Attempt 1	Shell 99 model	Solid 45 model
100μm sub+2diel 20μm+4*elec 10μm+2*PZT 50μm+2*mass 150μm		
W = 2cm, L = 5cm, Lm = 2/5*L	29.70	30.00
W = 2cm, L = 4.1cm, Lm = 2/5*L	44.50	44.90
W = 2cm, L = 4.05cm, Lm = 2/5*L	45.60	46.00
W = 2cm, L = 2.9cm, Lm = 2/5*L	89.50	90.60
W = 2cm, L = 2.8cm, Lm = 2/5*L	96.12	97.20
W = 2cm, L = 2.85cm, Lm = 2/5*L	92.70	93.70

Table 16 Attempt 1 finalized dimensions

After having chosen a suitable set of dimensions, an electro coupled ANSYS analysis was required to measure the produced voltage.



## Appendix D: Simple cantilever beam displacement and produced voltage results

In order to increase the generated voltage level, the cantilever beam structure was required to be adjusted. The first set of finalized dimensions presented in Appendix C, produced the generated voltage and displacement results depicted in table 17.

DEVICE A: 30Hz (acceleration at 15.44 m/s <sup>2</sup> )	Value
DMX (max deflection in m)	3.95x10 <sup>-4</sup>
SMN (minimum generated voltage in V)	-1.16x10 <sup>-1</sup>
SMX (maximum generated voltage in V)	1.16x10 <sup>-1</sup>

DEVICE B: 45Hz (acceleration at 8.611 m/s <sup>2</sup> )	Value
DMX	9.83x10 <sup>-5</sup>
SMN	-4.17x10 <sup>-2</sup>
SMX	4.17x10 <sup>-2</sup>

DEVICE C: 93Hz (acceleration at 2.01 m/s <sup>2</sup> )	Value
DMX	5.2x10 <sup>-6</sup>
SMN	-4x10 <sup>-3</sup>
SMX	4x10 <sup>-3</sup>

Table 17 Attempt 1 displacement and generated voltages

In an attempt to increase the generated voltage, a decision was made to increase the thickness of the mass layer to 200µm. Although greater voltage could possibly be achieved with an even thicker mass layer, any mass greater than 200µm would not be a suitable candidate for screen printing since bulk mass could be used instead.

Attempt 2 (increase mass to 200µm)	Shell 99 model	Solid 45 model
100µm sub+2diel 20µm+4*elec 10µm+2*PZT 50µm+2*mass 200µm		
W = 2cm, L = 4.9cm, Lm = 2/5*L	27.60	30.00
W = 2cm, L = 4.8cm, Lm = 2/5*L	28.70	44.90
W = 2cm, L = 4.7cm, Lm = 2/5*L	30.00	30.20
W = 2cm, L = 3.9cm, Lm = 2/5*L	43.70	90.60
W = 2cm, L = 3.8cm, Lm = 2/5*L	46.10	97.20
W = 2cm, L = 3.85cm, Lm = 2/5*L	44.90	45.30
W = 2cm, L = 2.7cm, Lm = 2/5*L	91.90	
W = 2cm, L = 2.65cm, Lm = 2/5*L	95.50	
W = 2cm, L = 2.67cm, Lm = 2/5*L	94.00	
W = 2cm, L = 2.68cm, Lm = 2/5*L	93.30	94.50
W = 2cm, L = 2.69cm, Lm = 2/5*L	92.60	93.80

DEVICE A: 30Hz (acceleration at 15.44 m/s <sup>2</sup> )	Value
DMX (max deflection in m)	3.83x10 <sup>-4</sup>
SMN (minimum generated voltage in V)	-1.24x10 <sup>-1</sup>
SMX (maximum generated voltage in V)	1.24x10 <sup>-1</sup>

DEVICE B: 45Hz (acceleration at 8.611 m/s <sup>2</sup> )	Value
DMX	9.84x10 <sup>-5</sup>
SMN	-4.40x10 <sup>-2</sup>
SMX	4.40x10 <sup>-2</sup>

DEVICE C: 93Hz (acceleration at 2.01 m/s <sup>2</sup> )	Value
DMX	5.16x10 <sup>-6</sup>
SMN	-4.33x10 <sup>-3</sup>
SMX	4.33x10 <sup>-3</sup>

Table 18 Attempt 2 displacement and generated voltages

A final approach was to increase the area of the mass layer to 50% of the beam length. Such a design alteration would lead to more mass existing on the beam structure. The generated voltage and displacement results can be observed in table 5.

## Appendix E: Simple cantilever beam structure efficiency and energy harvested power

The efficiency of a thick-film PZT layer can be calculated as follows:

k, electromechanical coupling coefficient:

$$k^2 = \frac{d^2 Y}{\varepsilon}$$

Where Y = Young's modulus and  $\varepsilon$  = Dielectric constant

For thick film material:

$$E = \text{relative dielectric} = 901 \times 8.85 \times 10^{-12} = 8 \times 10^{-9}$$

$$d_{33} = 131 \times 10^{-12}$$

$$Y = 2.6 \times 10^{10}$$

$$\text{Hence: } k_{33}^2 = 0.06 \Rightarrow k_{33} = 0.25$$

$$\text{Therefore for } d_{33} \text{ generator efficiency } \lambda_{\max} = \frac{k^2}{4-2k^2} = 0.016 \text{ or } 1.6\%$$

$$d_{31} = 60 \times 10^{-12}$$

$$\text{Hence: } k_{31}^2 = 0.0117 \Rightarrow k_{31} = 0.11$$

$$\text{Therefore for } d_{31} \text{ generator efficiency } \lambda_{\max} = \frac{k^2}{4-2k^2} = 0.003 \text{ or } 0.3\%$$

Energy harvested from thick film devices

$$P_{\text{avelec}} = P_{\text{avmech}} \times \lambda_{\max} = \frac{m \times W_n \times A \times Z_{\max}}{2} \times \lambda_{\max}$$

Where mass m is calculated based upon an assumed density value for the screen printed tungsten layer of  $15000 \text{ kg/m}^3$ ,  $W_n$  is frequency of operation, A is applied acceleration and  $Z_{\max}$  is the peak-to-peak displacement. Actual displacement would depend upon the resonance quality factor [3].

Device	Frequency (Hz)	Length (cm)	Width (cm)	Maximum peak amplitude (mm)	Printed mass, m(g)	Predicted power ( $\mu\text{W}$ )
A	30	4.68	2	5	2.8	122
B	45	3.84	2	3	2.3	50
C	93	2.68	2	2.5	1.6	10

Table 19 Device design parameters [26]

## Appendix F: Individual screen designs

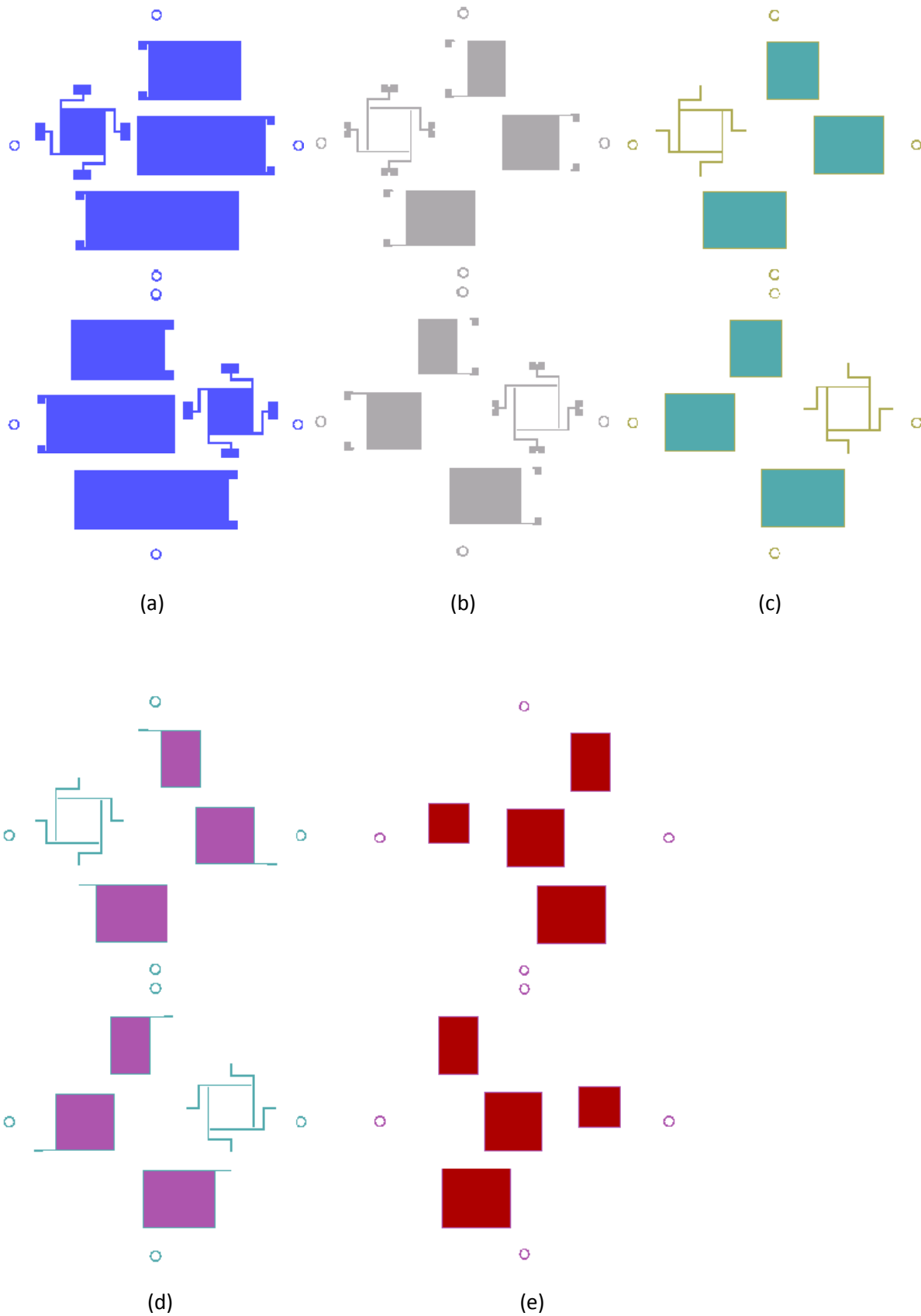


Figure 36 Substrate 1 associated screen designs: a) dielectric screen, b) bottom electrode screen, c) PZT screen, d) Top electrode screen, e) Mass screen

In addition, two IDT electrode screens were designed in order to create a device which operates using the  $d_{33}$  PZT coefficient. Figure 37 depicts a screen consisting of a series of 150 $\mu\text{m}$  thick electrode “fingers”. Figure 38 depicts a second IDT screen where the distance between the electrode “fingers” has been increased to 200 $\mu\text{m}$ .

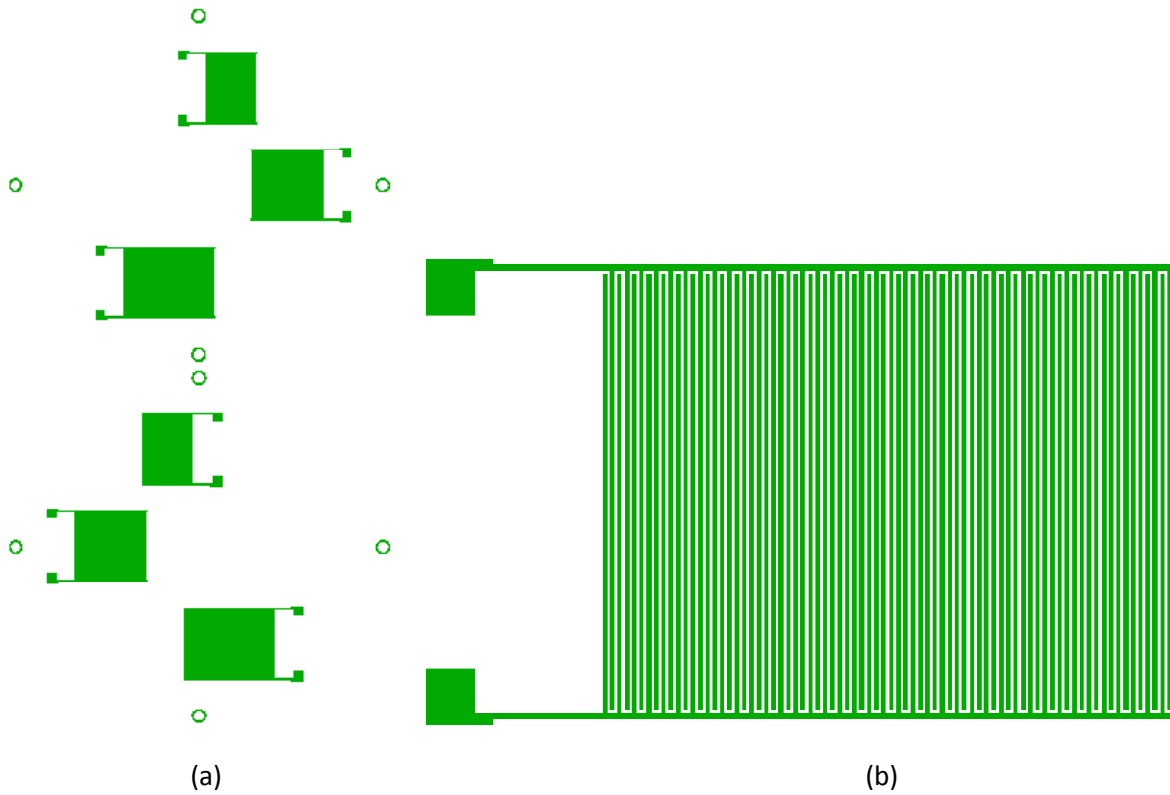


Figure 37 a) IDT electrode screen b) 30Hz cantilever beam IDT electrode screen section

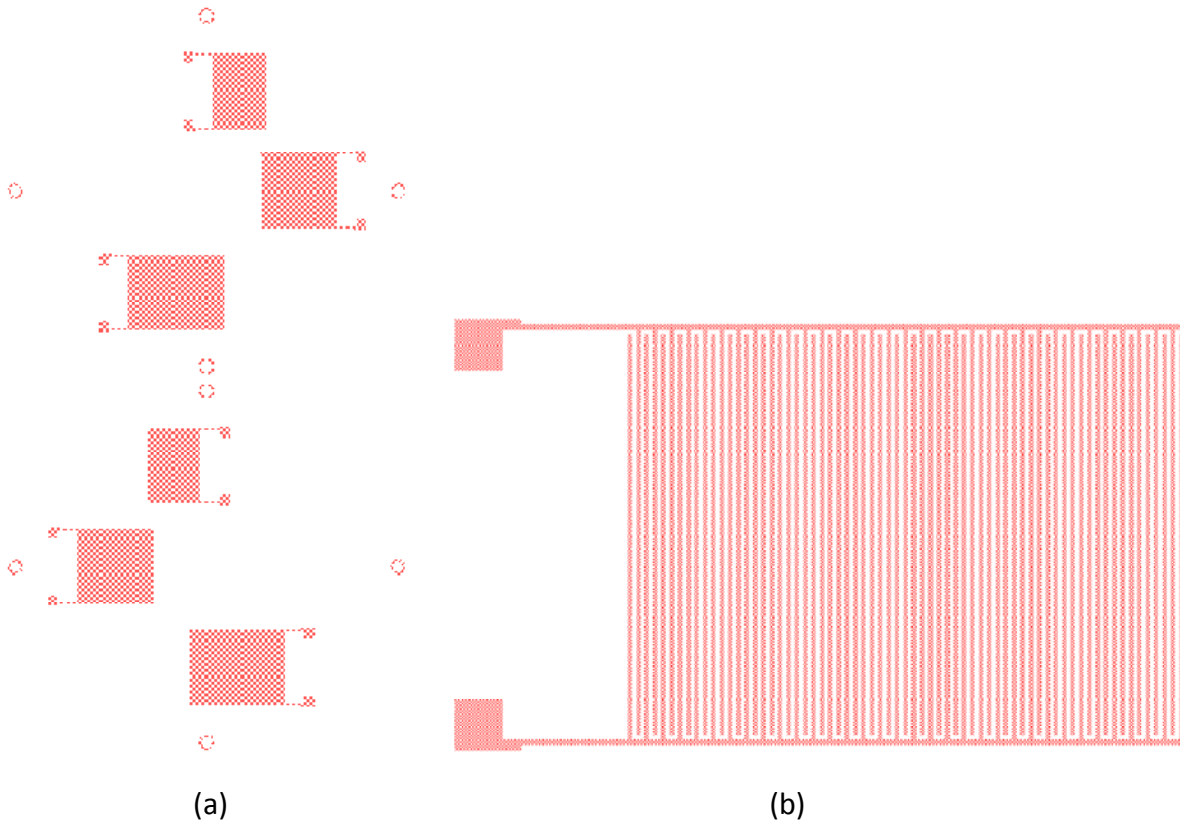


Figure 38 a) IDT electrode screen 200 $\mu\text{m}$  distance between electrodes b) 30Hz cantilever beam IDT electrode screen section

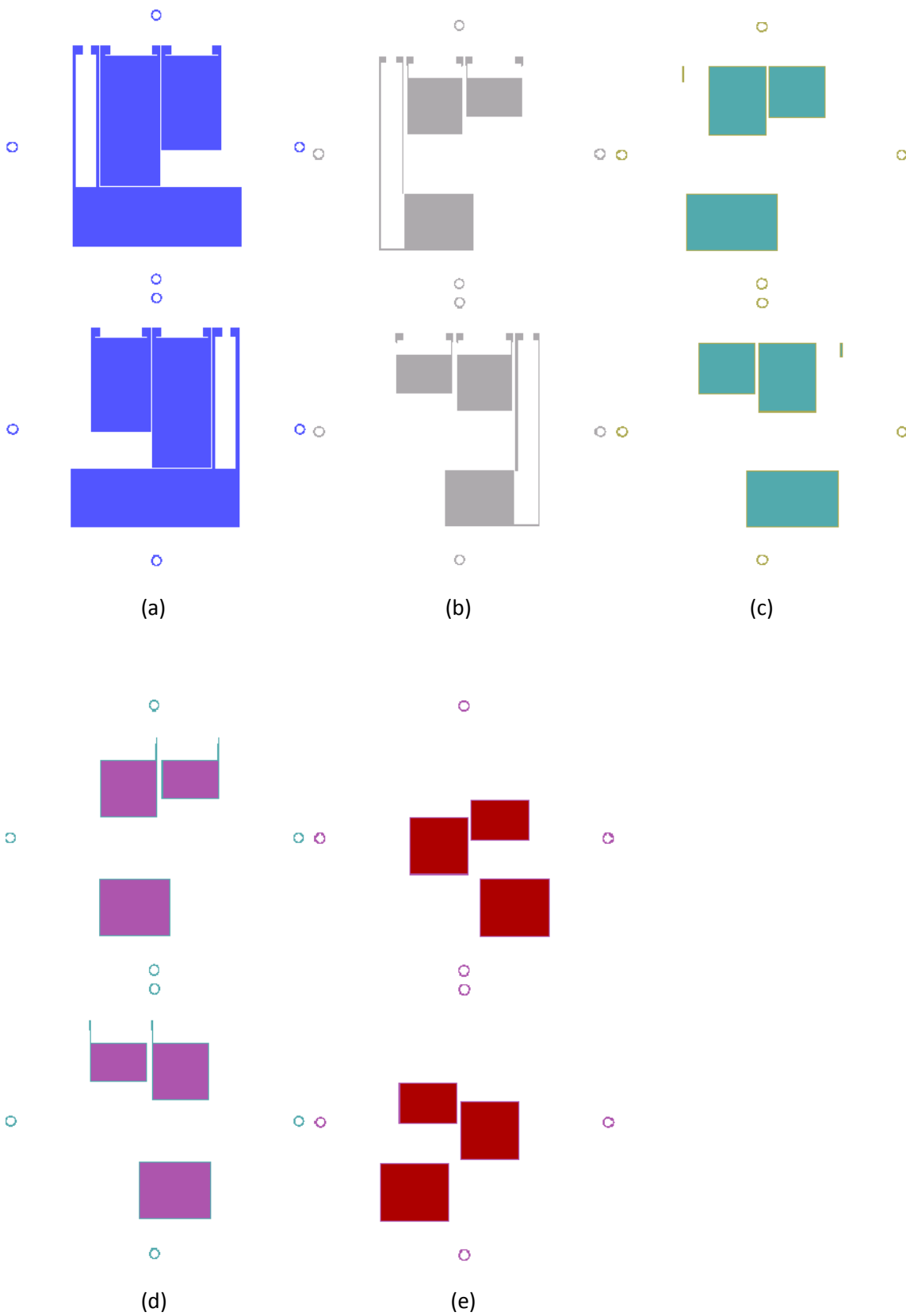


Figure 39 Substrate 2 associated screen designs: a) dielectric screen, b) bottom electrode screen, c) PZT screen, d) Top electrode screen, e) Mass screen

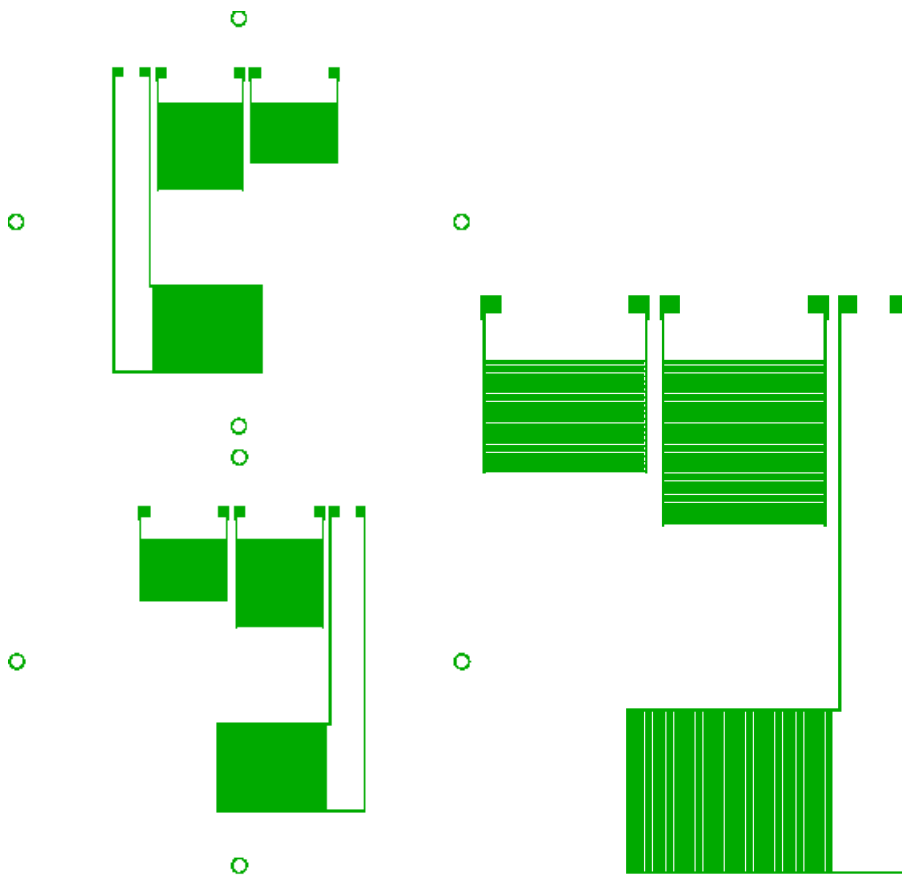


Figure 40 Substrate 2 IDT electrode screen

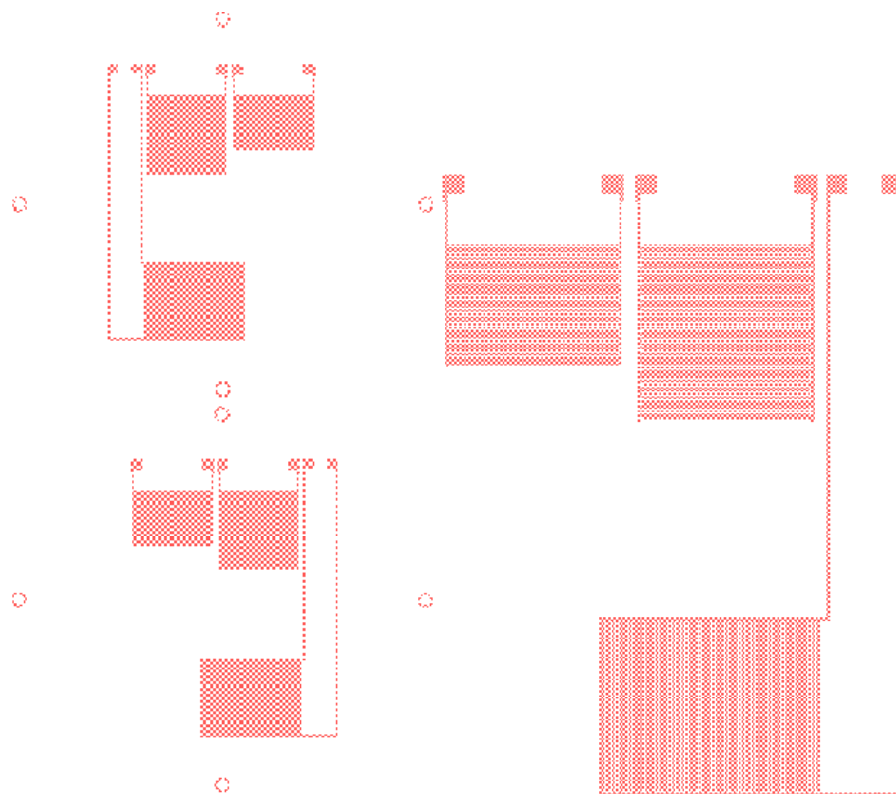
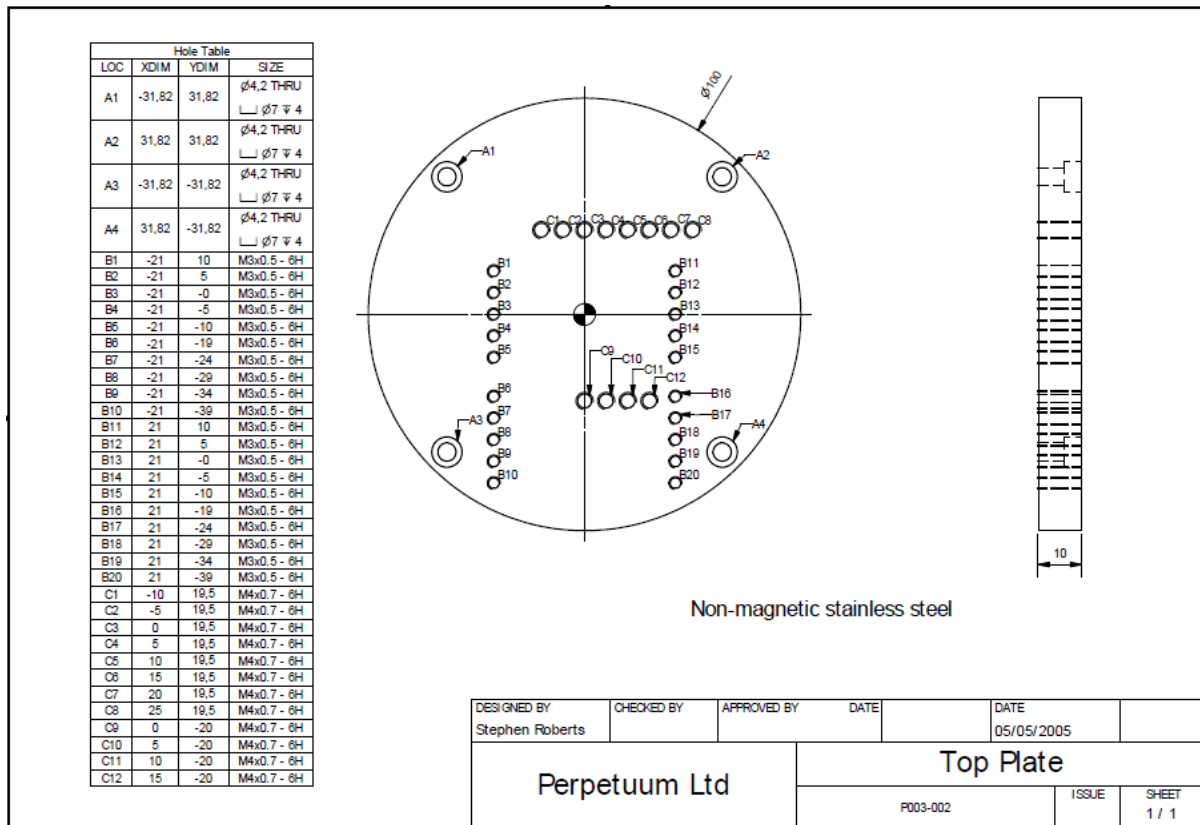


Figure 41 Substrate 2 IDT electrode screen 200μm distance between electrodes

## Appendix G: Top plate schematic



### Figure 42 Top plate schematic

## Appendix H: Test clamp design dimensions

### a) Cantilever beam clamp design

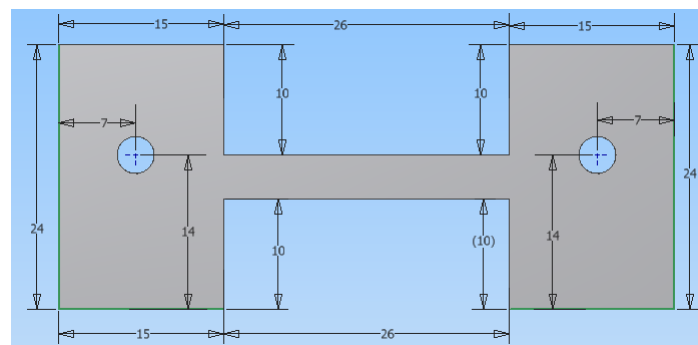


**Figure 43 Basic cantilever beam clamp dimensions**

Extruded for 5mm for top clamp piece and 18mm for bottom clamp piece.



## b) Three beam cantilever clamp design

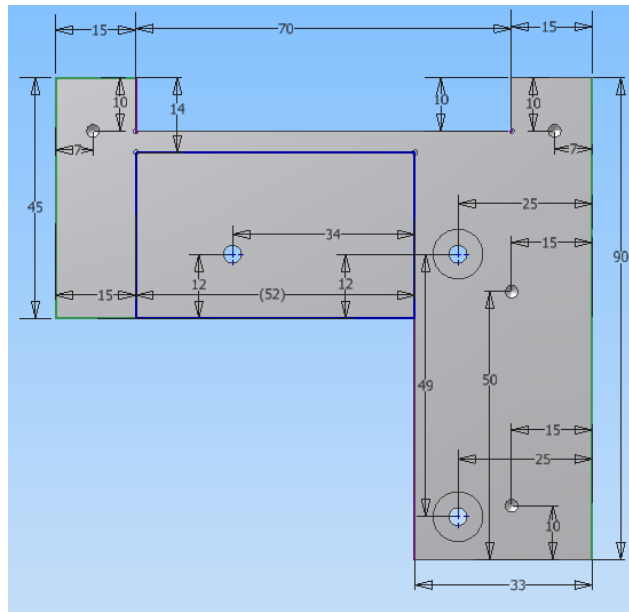


Figure 44 Three beam cantilever clamp bottom piece dimensions

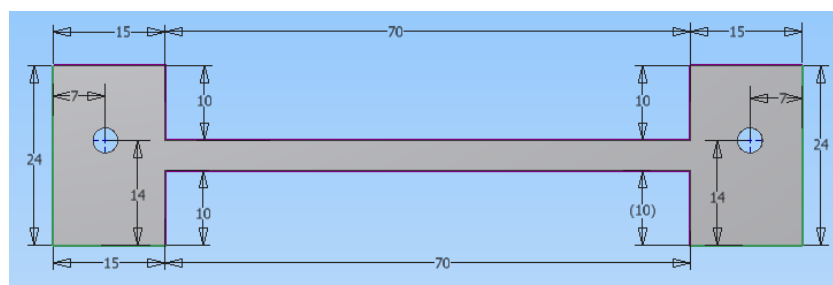
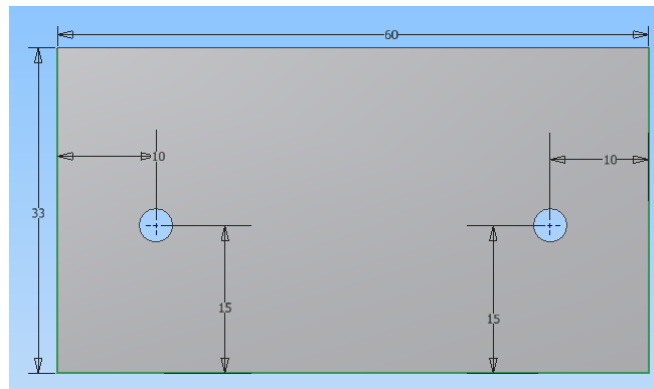


Figure 45 Three beam cantilever clamp top pieces dimensions

Extruded for 20mm for bottom clamp piece and 5mm for top clamp pieces.

### c) Meandrical clamp design

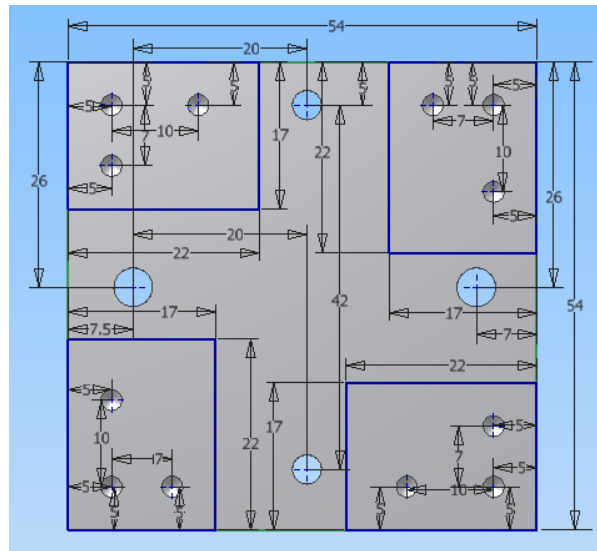


Figure 46 Meandrical device clamp design bottom piece dimensions

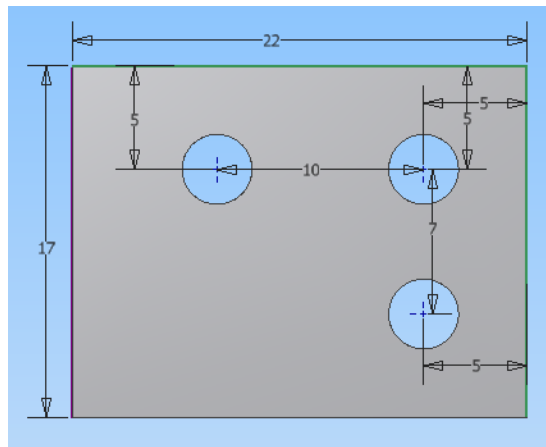


Figure 47 Meandrical device clamp design top pieces dimensions

Extruded for 20mm for bottom clamp piece and 5mm for top clamp pieces.

## Appendix I: Mass ink deposition

During formulation of the tungsten ink, the following ingredient percentages were used:

a) Glass based ink

Paste formulation	Tungsten: 4-6 µm particle size (g)	Tungsten: 1 µm particle size (g)	CF7575 Glass (g)	V400 Vehicle (ml)
10% glass ink	29	61	10	18.5
20% glass ink	25.6	54.4	20	13
30% glass ink	22.4	47.6	30	14.5
60% glass ink	12.8	27.2	60	14.5

Table 20 Glass based mass ink formulations

All printed layers were dried at 140 °C and fired at 850 °C. Figure 48 consists of example images from fired alumina substrates.

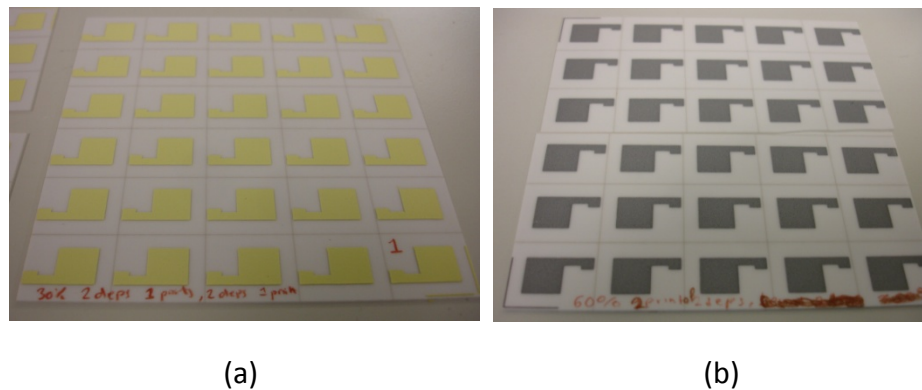


Figure 48 Printed mass inks: a) 30% glass paste print, b) 60% glass paste print

As it can be observed from figure 48 a), the results acquired from the print of the 30% glass ink were unsatisfactory since the resulting layer was extremely brittle thus making any thickness or density measurement impossible. The same solid behaviour was observed for the print of the 10% and 20% glass inks. A noticeable improvement occurred for the printing of the 60% glass ink. The structure consisted of a solid layer with no apparent brittleness, which could not easily be damaged with a scalpel.

Density calculation:

Alumina tile weight: 24.39g

Alumina with printed structure: 25.59g

Printed structure surface: 1cm<sup>2</sup>

Average thickness of printed structure: 118.75µm

$$\rho = \frac{m}{V} = \frac{m}{W * L * T}$$

where  $m$  = mass,  $W$  = width of structure,  $L$  = length of structure,  $T$  = thickness of structure

$$\text{Thus } \rho = 3.36 \times 10^3 \text{ kg/m}^3$$

Glass based tungsten ink trials were made with the assistance of Miss Charlene Nicoleau and Dr Russel Torah

b) Polymer based ink

Paste formulation	Tungsten: 4-6 $\mu\text{m}$ particle size (g)	Tungsten: 1 $\mu\text{m}$ particle size (g)	ESL 240-SB polymer (g)	V400 Vehicle (ml)
polymer ink	27.2	57.8	15	5.2
1 $\mu\text{m}$ polymer ink		85	15	7.4

Table 21 Polymer based mass ink formulations

All printed layers were dried at 140 °C and cured at 215 °C. For both inks the resulting structures showed no evidence of brittleness.

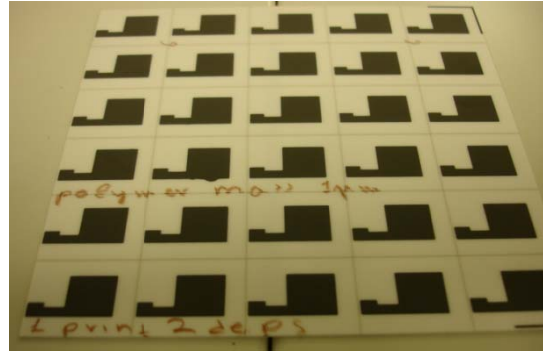
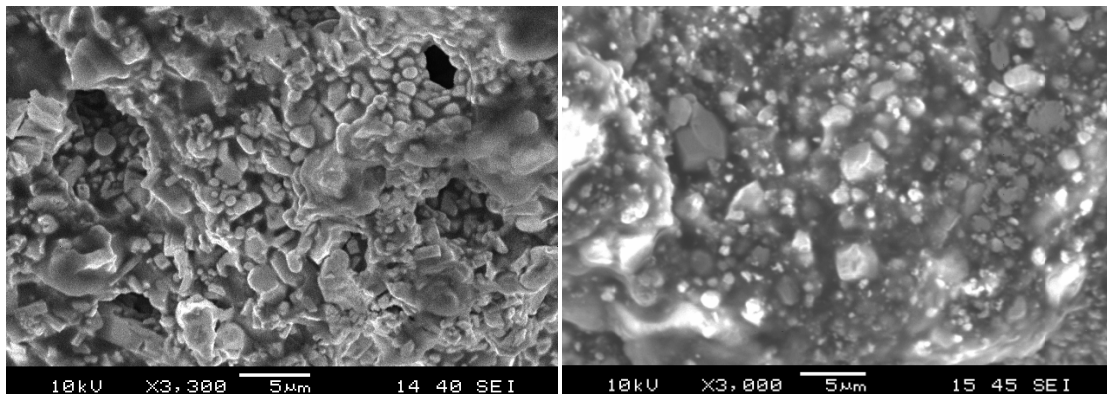


Figure 49 Polymer based tungsten mass structures

Mass ink	Printed Layers	Thickness ( $\mu\text{m}$ )	Density ( $\text{kg}/\text{m}^3$ )
polymer ink	1	42.5	5647
	2	65.25	7050
1 $\mu\text{m}$ polymer ink	1	34.5	4600
	2	57.5	5900

Table 22 Measured densities for polymer ink



(a)

(b)

Figure 50 Tungsten ink S.E.M. pictures: a) 60% glass ink b) Variable particle size polymer ink

As it can be observed from the S.E.M. pictures of figure 50, the glass based ink was much more porous compared to the polymer ink which resulted to a significantly lower density.

## Appendix J: Device testing results

a) 45 Hz co fired cantilever IDT device

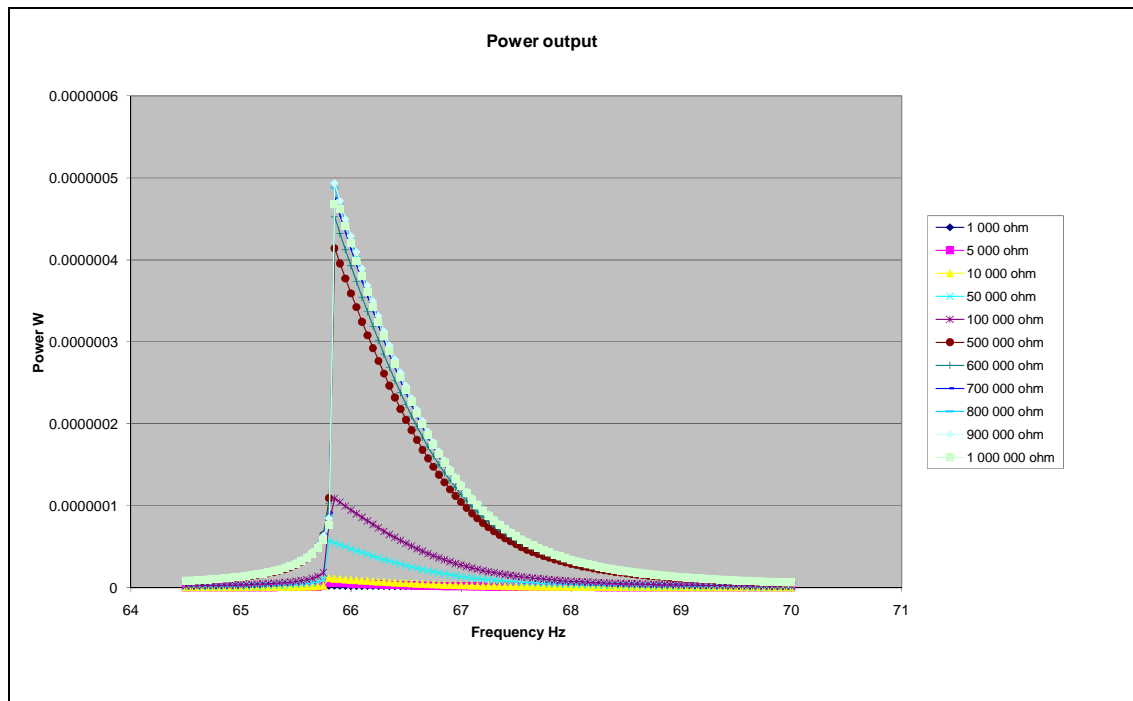


Figure 51 45 Hz IDT cantilever beam output power at 100mG acceleration

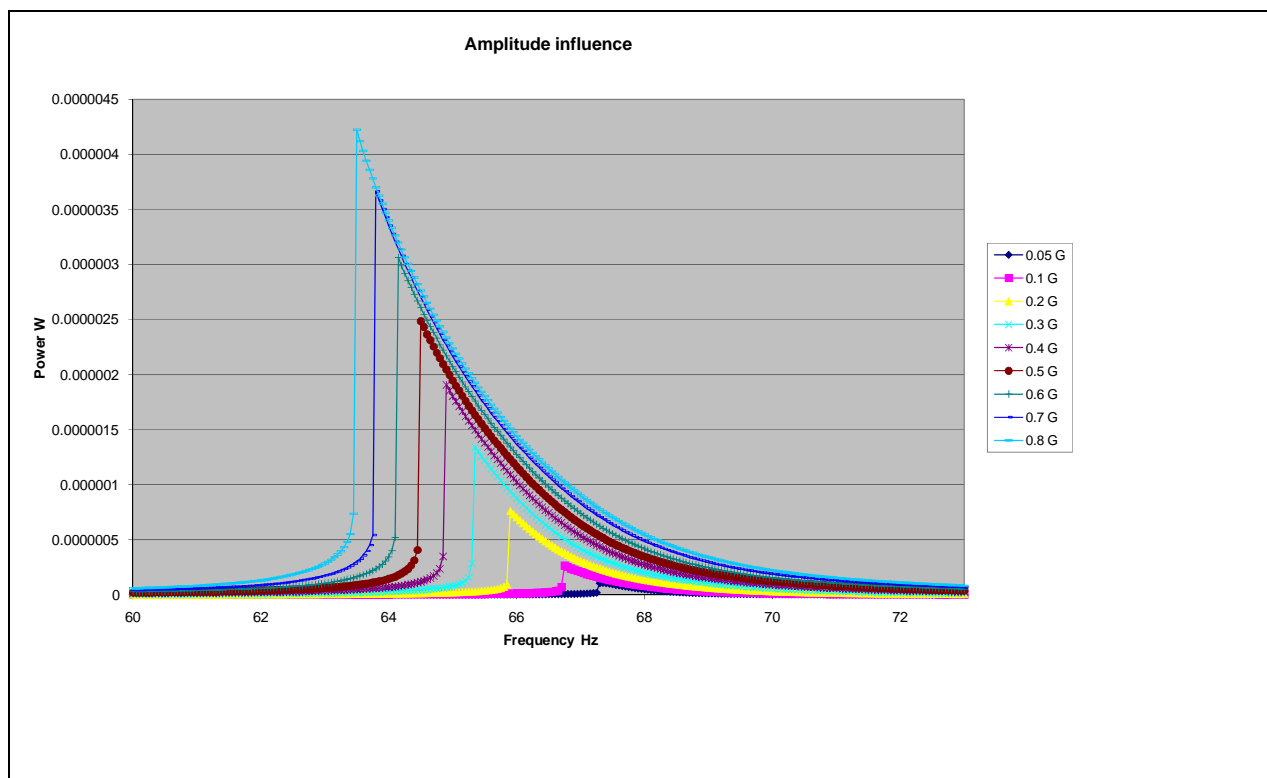


Figure 52 45Hz IDT cantilever beam increased power output at increased acceleration under optimum load resistance

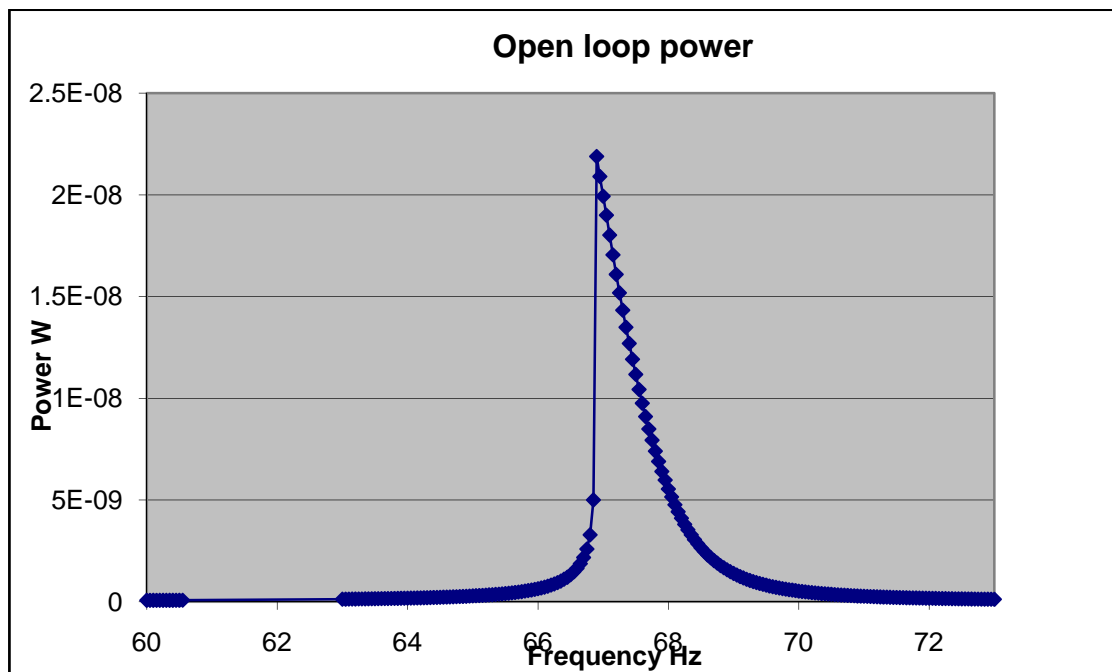


Figure 53 45Hz IDT cantilever beam open loop power at 100mG acceleration with 9Mohm resistance load

b) 30Hz cantilever beam with tungsten mass

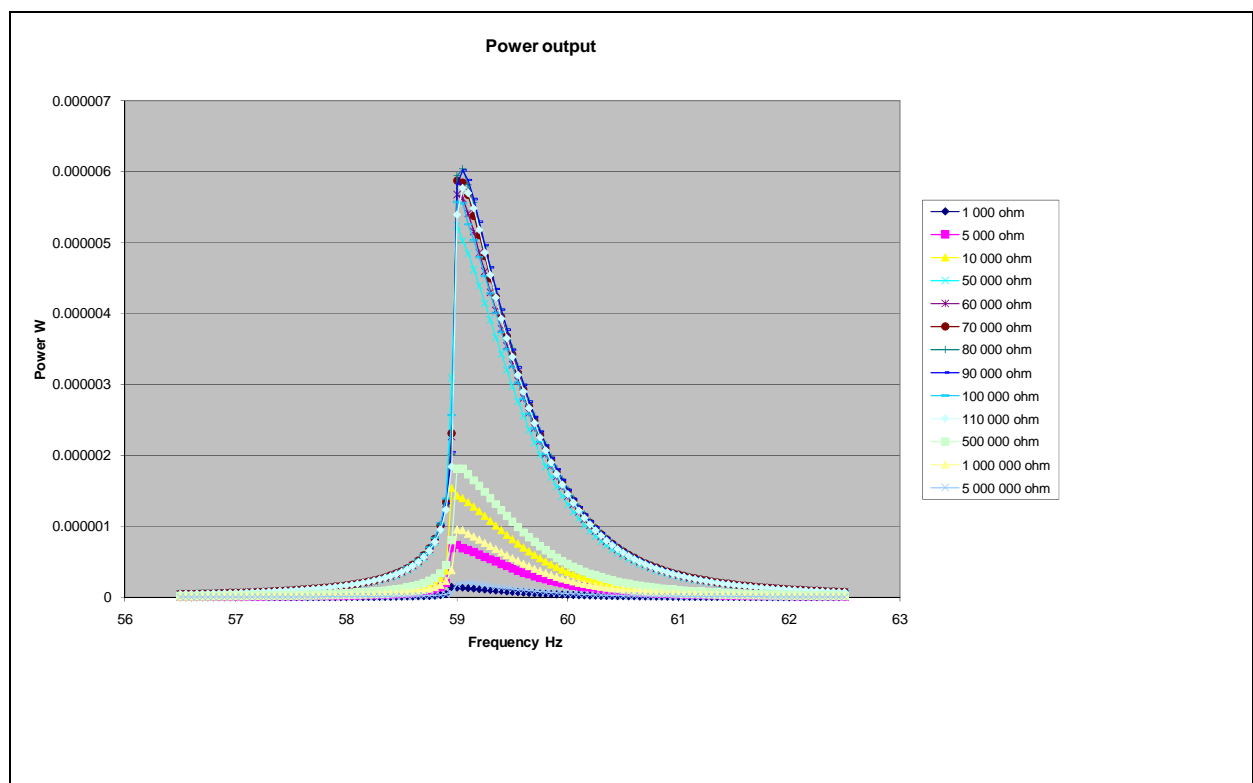


Figure 54 30Hz cantilever beam output power at 100mG acceleration

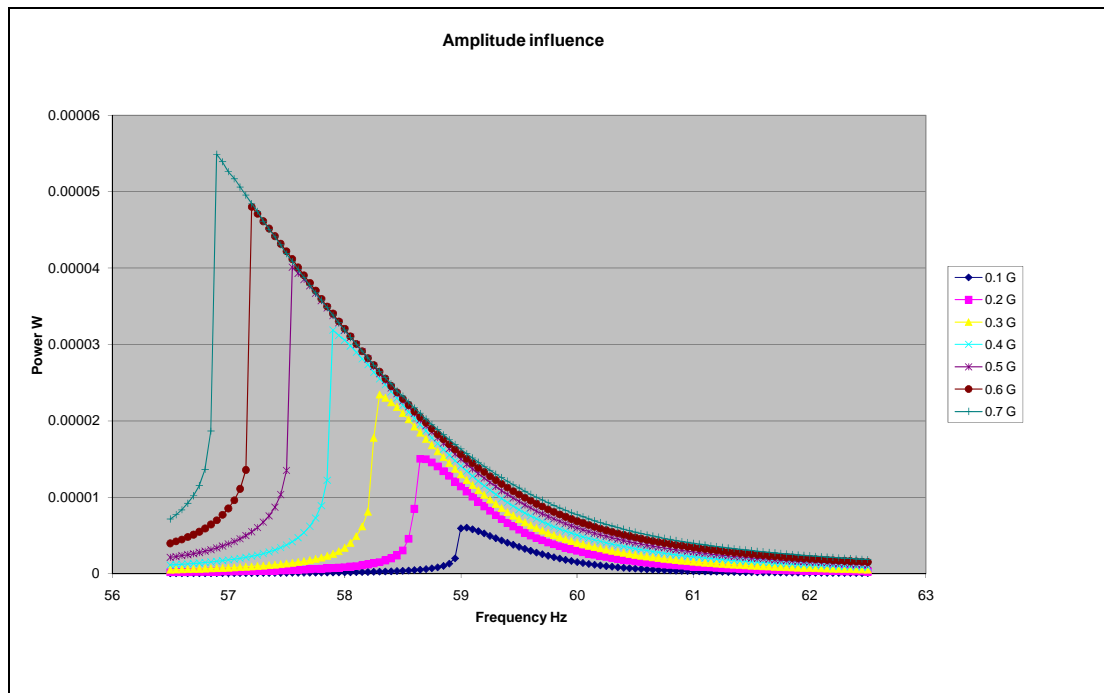


Figure 55 30Hz cantilever beam increased power output at increased acceleration under optimum load resistance

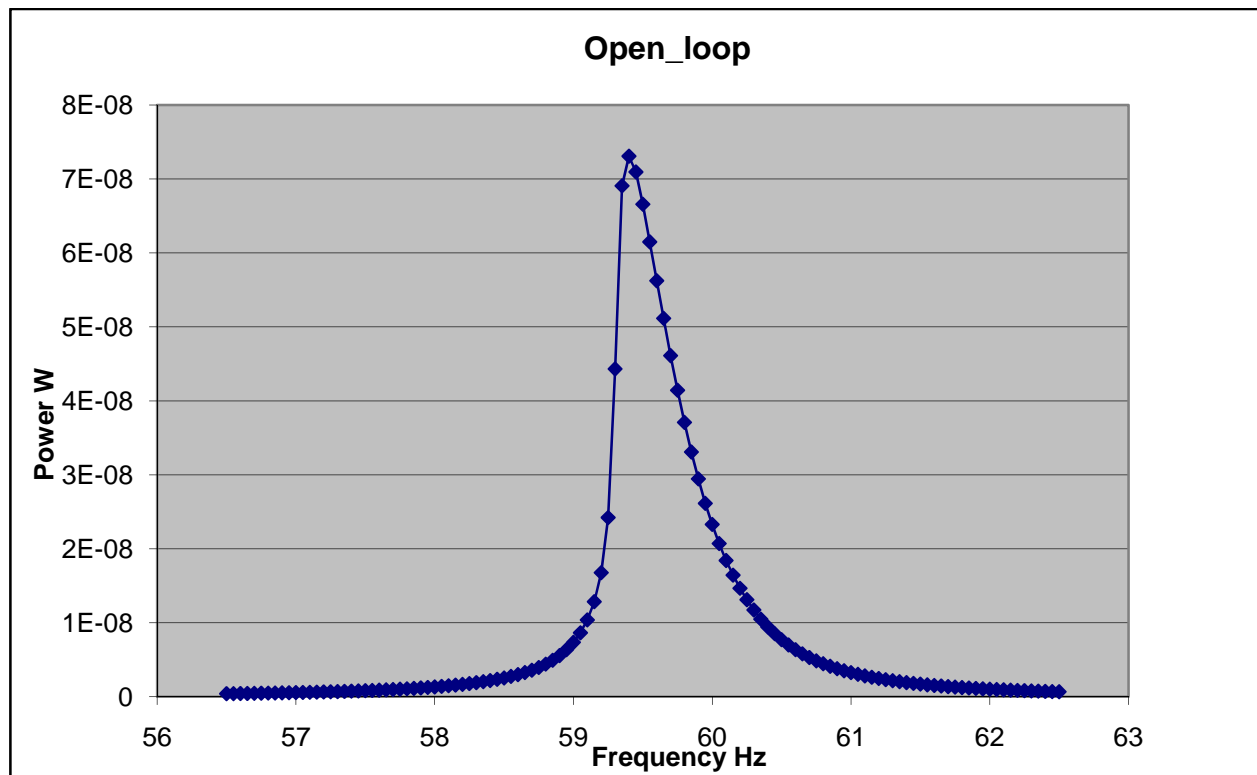


Figure 56 30Hz cantilever beam open loop power at 100mG acceleration with 5Mohm resistance load

c) 30Hz cantilever beam with 1.62g glued mass

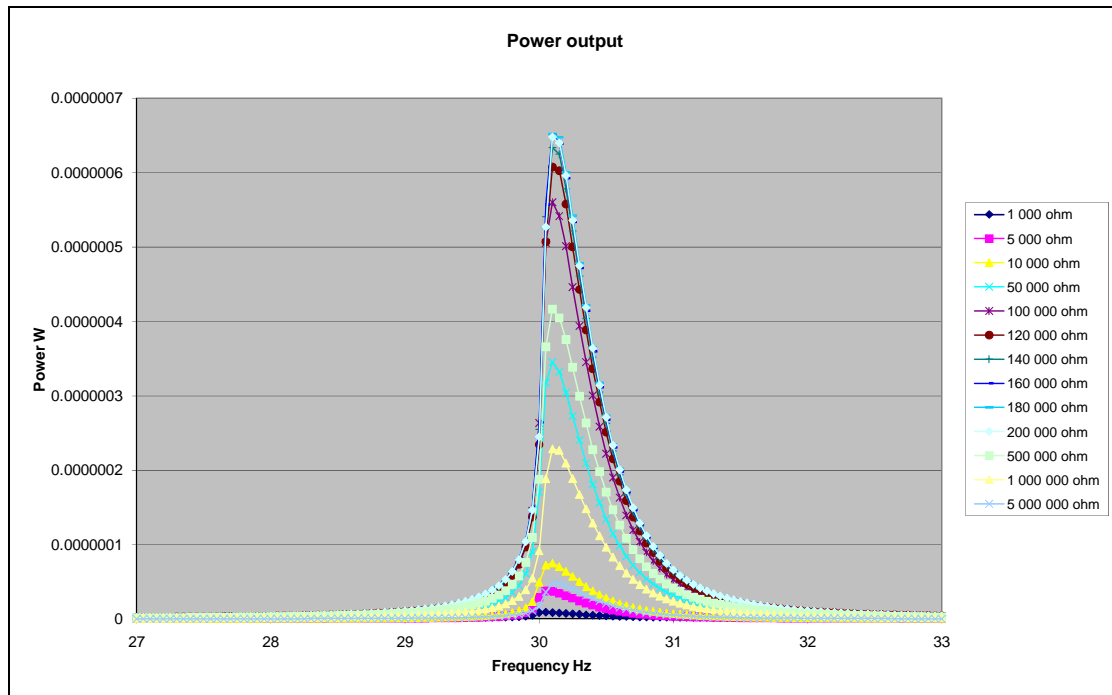


Figure 57 30Hz cantilever beam with glued mass, output power at 100mG acceleration

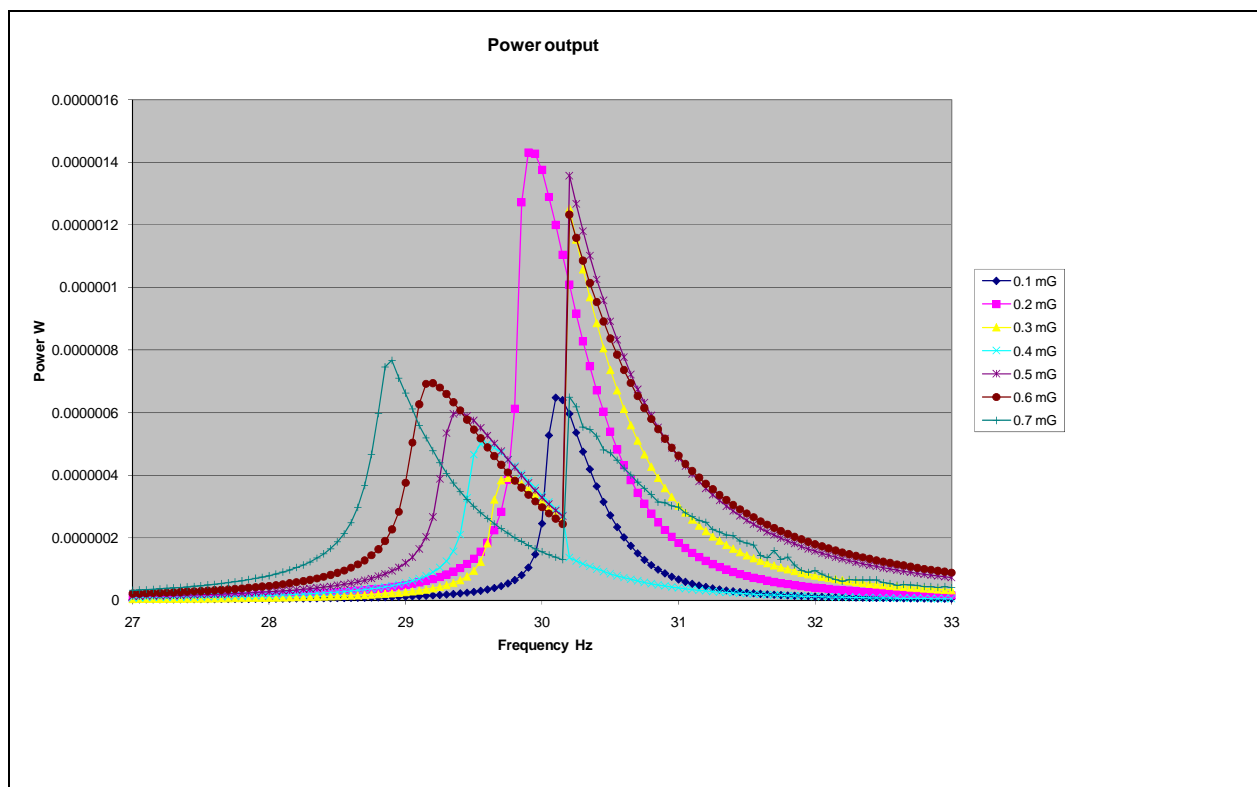


Figure 58 30Hz cantilever beam with glued mass, increased power output at increased acceleration under optimum load resistance



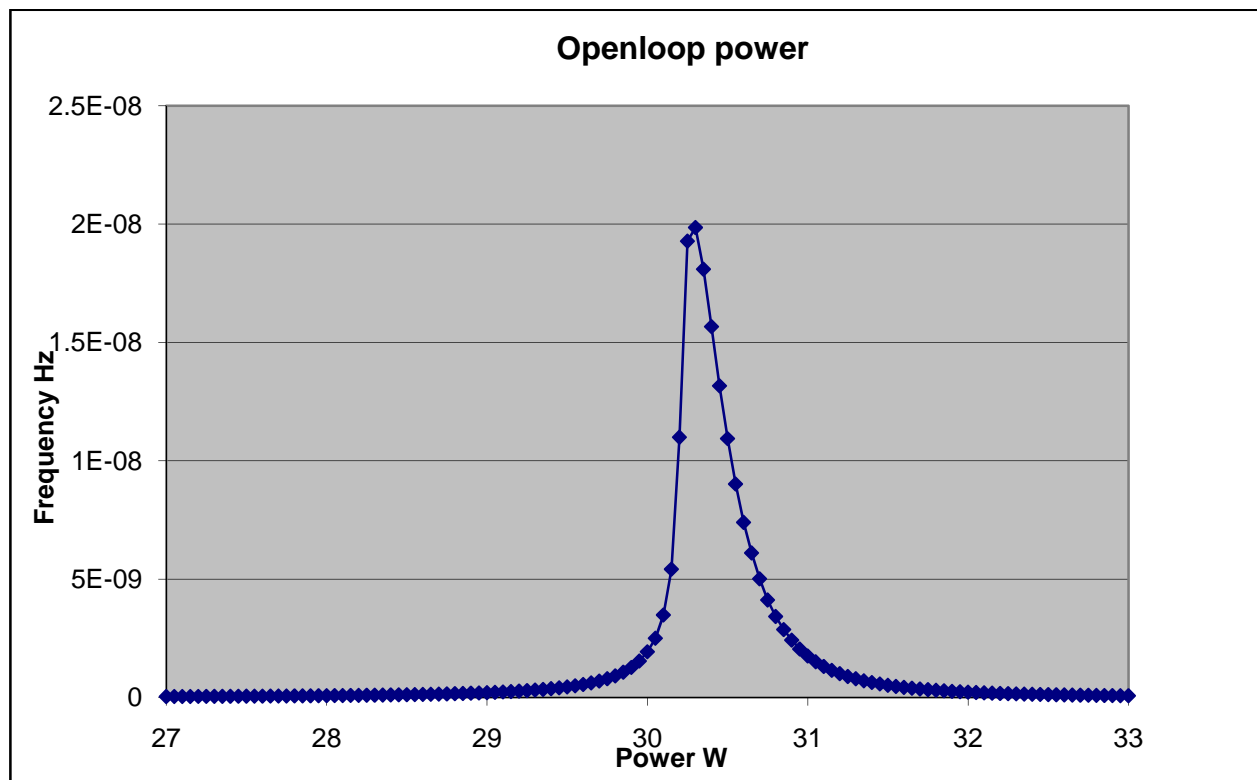


Figure 59 30Hz cantilever beam with glued mass, open loop power at 100mG acceleration with 5Mohm resistance load

#### Appendix CD: CD contents

Root folder	Contents
ANSYS models	Solid 45 model, shell 99 model, meandrical Solid 45 model
L-edit	Screen designs, substrate etch masks, pictures from printed layers, substrate Gerber file exports, S.E.M. mass ink pictures, screen printer pictures
Autodesk Inventor	Clamp designs, substrate holder
Testing	Test results, pictures from testing procedures

Table 23 CD contents

## IX. References

- [1] Rabaey et al 2000, Gates 2002, Wang et al 2002, Hitachi mu-Chip 2003
- [2] Raghunathan V, Schurgers C, Park S and Skrivastava M B 2002, Energy-aware wireless micro sensor networks IEEE Signal Process. Mag. 19 40-50
- [3] Shadrach Joseph Roundy 2003, Energy Scavenging for Wireless Sensor Nodes with a Focus on Vibration to Electricity Conversion, Berkeley University of California
- [4] Shearwood C and Yates R B 1997 Development of an electromagnetic micro-generator Electron. Lett. 33 1883-4
- [5] Amirtharajah R and Chandrakasan A P 1998 Self-powered signal processing using vibration-based power generation IEEE J. Solid-State Circuits 33 687-95
- [6] Ching N H, Wong H Y, Li W J, Leong P H W and Wen Z 2002 A laser-micro machined multi-modal resonating power transducer for wireless sensing systems Sensors Actuators A 97/98 685-90
- [7] El-hami M, Glynne-Jones P, White N M, Hill M, Beeby S, James E, Brown A D and Ross J N 2001 Design and fabrication of a new vibration-based electromechanical power generator Sensors Actuators A 92 335-42
- [8] Meninger S, Mur-Miranda J O, Amirtharajah R, Chandrakasan A P and Lang J H 2001 Vibration-to-electric energy conversion IEEE Trans. Very Large Scale Integr. (VLSI) Syst. 9 64-76
- [9] Roundy S, Wright P K and Pister K S J 2002, Micro-electrostatic vibration-to-electricity converters ASME IMECE (New Orleans, LA, Nov. 2002)
- [10] Miyazaki M, Tanaka H, Ono G, Nagano T, Ohkubo N, Kawahara T and Yano K 2003 Electric-energy generation using variable-capacitive resonator for power-free LSI: efficiency analysis and fundamental experiment ISLPED 2003 (Seoul, Korea, Aug.2003)
- [11] Schmidt V H 1986 Theoretical electrical power output per unit volume of PVF2 and mechanical-to-electrical conversion efficiency as functions of frequency Proc. 6<sup>th</sup> IEEE Int. Symp. On Applications of Ferroelectrics pp 538-42
- [12] Shenck N S and Paradiso J A 2001 Energy scavenging with shoe-mounted piezoelectrics IEEE Micro 21 30-41
- [13] Glynne-Jones P, Beeby S P, James E P and White N M 2001, The modelling of a piezoelectric vibration powered generator for Microsystems Transducers 01/Eurosensors XV (June 2001)
- [14] Ottman G K, Hofmann H F and Lesieutre G A 2003 Optimized piezoelectric energy harvesting circuit using step-down converter in discontinuous conduction mode, IEEE Trans. Power Electron. 18 696-703
- [15] Roundy S, Wright P K and Rabaey J 2003 A study of low level vibrations as a power source for wireless sensor nodes Comput. Commun. 26 1131-44
- [16] P Glynne-Jones, SP Beeby, NM White. Towards a piezoelectric Vibration-Powered Micro generator, Department of Electronics and Computer Science, University of Southampton

- [17] R.N. Torah, S.P. Beeby, M.J. Tudor, T.O' Donnell, S.Roy, Development of a Cantilever Beam Generator Employing Vibration Energy Harvesting, University of Southampton, School of Electronics and Computer Science
- [18] Roundy S, Wright P K and Rabaey J M 2003, Energy Scavenging for Wireless Sensor Networks (Norwell, MA: Kluwer-Academic)
- [19] S P Beeby, M J Tudor and N M White, Energy harvesting vibration sources for Microsystems applications, School of Electronics and Computer Science, University of Southampton
- [20] European Commission, Seventh Framework Programme Theme 7 Transport, TRIADE project
- [21] J.E. Brignell, N.M. White, A.W.J Cranny, IEE Proc. I. 135(4), 77-84 (1988)
- [22] R. N. Torah, S. P. Beeby, M. J. Tudor, N. W. White, Thick-film piezoceramics and devices
- [23] C. Robertson, R. D. Shipton, D. R. Gray, Sens. Rev. 19(1), 33-36 (1999)
- [24] Peter Glynne-Jones, Vibration powered generators for self-powered Microsystems, department of electronics and computer science, University of Southampton
- [25] Course in FEM-ANSYS Classic Geometric Modelling, Computational Mechanics, AAU, Esbjerg
- [26] M Stamos, C Nicoleau, R Torah, M Tudor, N Harris, Andrzej Niewiadomski, S Beeby, Abstract of Screen-printed piezoelectric generator for helicopter health and usage monitoring system, University of Southampton
- [27] <http://www.azom.com/Details.asp?ArticleID=996>
- [28] <http://www.valleydesign.com/pyrex.htm>
- [29] <http://www.memsnet.org/material>
- [30] [http://www.ctscorp.com/components/pzt/downloads/PZT\\_5Aand5H.pdf](http://www.ctscorp.com/components/pzt/downloads/PZT_5Aand5H.pdf)
- [31] H Jaffe, D A Berlincourt, Piezoelectric Transducer Materials
- [32] ANSYS Modelling and Meshing Guide for ANSYS 10.0
- [33] Wire cloth for screen printing guide, provided by BOPP SD Applications
- [34] R Sandberg, W Svendsen, K Molhave, A Boisen, Temperature and pressure dependence of resonance in multi-layer micro cantilevers, Institute of Physics Publishing, J. Micromech. Microeng. 15 (2005) 1454-1458